Magic continuum in multi-moiré twisted trilayer graphene

Li-Qiao Xia,[1,*] Aviram Uri,[1,†] Jiaojie Yan,[2,†] Aaron Sharpe,[3,4,†] Filippo Gaggioli,[1] Nicole S. Ticea,[5] Julian May-Mann,[3] Kenji Watanabe,[6] Takashi Taniguchi,[7] Liang Fu,[1] Trithep Devakul,[3] Jurgen H. Smet,[2] and Pablo Jarillo-Herrero[1,‡]

[1] *Department of Physics, Massachusetts Institute of Technology, Cambridge, Massachusetts 02139, USA*
[2] *Max Planck Institute for Solid State Research, 70659, Stuttgart, Germany*
[3] *Department of Physics, Stanford University, Stanford, California 94305, USA*
[4] *Stanford Institute for Materials and Energy Sciences, SLAC National Accelerator Laboratory, Menlo Park, California 94025, USA*
[5] *Department of Applied Physics, Stanford University, Stanford, California 94305, USA*
[6] *Research Center for Electronic and Optical Materials, National Institute for Materials Science, 1-1 Namiki, Tsukuba 305-0044, Japan*
[7] *Research Center for Materials Nanoarchitectonics, National Institute for Materials Science, 1-1 Namiki, Tsukuba 305-0044, Japan*

(Dated: September 5, 2025)

Moiré lattices provide a highly tunable platform for exploring the interplay between electronic correlations and band topology [1]. Introducing a second moiré pattern extends this paradigm: interference between the two moiré patterns produces a supermoiré modulation, opening a route to further tailor electronic properties. Twisted trilayer graphene generally exemplifies such a system: two distinct moiré patterns arise from the relative twists between adjacent graphene layers. Here, we report the observation of correlated phenomena across a wide range of twisted trilayer graphene devices whose twist angles lie along two continuous lines in the twist-angle parameter space [2–5]. Depending on the degree of lattice relaxation, twisted trilayer graphene falls into two classes [4]: moiré polycrystals [6, 7], composed of periodic domains with locally commensurate moiré order, and moiré quasicrystals, characterized by smoothly varying local moiré configurations [8]. In helically twisted moiré polycrystals, we observe an anomalous Hall effect, consistent with topological bands arising from domains with broken xy-inversion symmetry. In contrast, superconductivity appears generically in our moiré quasicrystals. A subset of these systems exhibits signatures of spatially modulated superconductivity, which we attribute to the supermoiré structure. Our findings uncover the organizing principles of the observed correlated phases in twisted trilayer graphene, highlight the critical roles of the supermoiré modulation and lattice relaxation, and suggest a broader framework in which magic conditions arise not as isolated points but as extended manifolds within the multi-dimensional twist-angle space of complex moiré materials.

A small mismatch between the lattice vectors of adjacent two-dimensional (2D) materials generates a moiré pattern: an emergent superlattice that modulates the interlayer atomic registry on length scales much larger than the atomic lattice constant. The twist angle degree of freedom enables continuous tuning of moiré potentials and hence electronic structures, establishing moiré materials as a designer platform for novel quantum phenomena, including correlated insulating states [9], superconductivity [10], and integer and fractional quantum anomalous Hall effects [11, 12]. Most prior studies have focused on systems with a single moiré pattern, such as twisted bilayer graphene, where correlated states emerge near discrete "magic" twist angles that yield flat bands. Multi-moiré systems, which host two or more distinct moiré patterns, provide additional twist angle degrees of freedom and enable the exploration of magic conditions in higher-dimensional twist-angle spaces.

Here, we focus on one of the simplest multi-moiré systems—twisted trilayer graphene (TTG), in which three graphene monolayers are stacked with two independent twist angles: θ_{12} between layers 1 and 2, and θ_{23} between layers 2 and 3 (Fig. **1a**). This trilayer stacking yields either a helical or alternating twist configuration, depending on whether θ_{12} and θ_{23} have the same or opposite signs, respectively. Except in the special cases of mirror-symmetric TTG ($\theta_{12} = -\theta_{23}$) and twisted monolayer-bilayer graphene ($\theta_{12} = 0$ or $\theta_{23} = 0$), TTG generally hosts two incommensurate moiré patterns, resulting in a rich and tunable multi-moiré landscape. Previous studies reported contrasting correlated phenomena in several specific configurations of TTG, including superconductivity near $(\theta_{12}, \theta_{23}) \approx (1.6°, -1.6°)$ or $(1.4°, -1.9°)$ [8, 13, 14], and an anomalous Hall effect (AHE) near $(\theta_{12}, \theta_{23}) \approx (1.8°, 1.8°)$ [6] (these works are denoted as dark green circles in Fig. **1a**). However, the underlying principles that govern the ground states of different twist angle configurations, and the rules that dictate where correlated phenomena arise in the two-angle space, remain unclear.

In this work, we observed correlated ground states in seven multi-moiré TTG devices with new twist angle configurations, denoted as red circles in Fig. **1a** (see also Methods A, Methods B, and Extended Data Fig. **1**). Remarkably, all samples with twist angles near two con-

* These authors contributed equally.; xialq@mit.edu
† These authors contributed equally.
‡ pjarillo@mit.edu

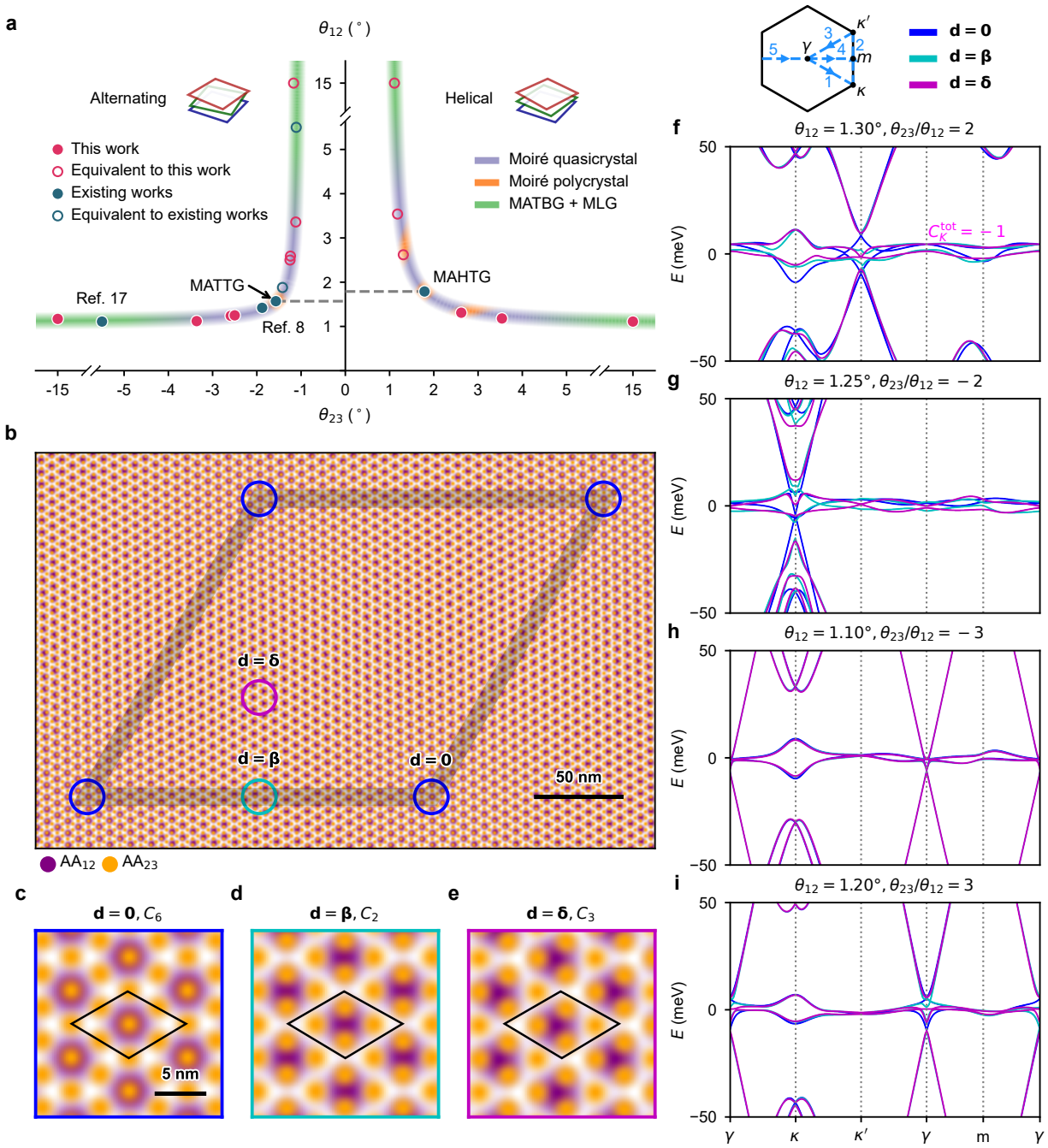

Fig. 1. **Magic continuum in TTG. a**, Structural parameter space of TTG. Solid circles and their hollow equivalents denote twist-angle combinations where strong correlations were observed in previous works (dark green) and in the present study (red). They lie on two branches of a magic continuum in the parameter space. Based on the degree of lattice relaxation, TTG can be categorized into moiré quasicrystals (purple-shaded regions) and moiré polycrystals (orange-shaded regions). For large values of $|\theta_{12}|$ ($|\theta_{23}|$) along the magic continuum, one of the layers becomes electronically decoupled and the other two layers form magic-angle twisted bilayer graphene where $|\theta_{23}|$ ($|\theta_{12}|$) ~ 1.1° (green-shaded regions). MATBG, magic-angle twisted bilayer graphene; MLG, monolayer graphene; MATTG, magic-angle (alternating and mirror-symmetric) twisted trilayer graphene; MAHTG, magic-angle helical trilayer graphene. **b**, Unrelaxed structure of TTG with $(\theta_{12}, \theta_{23}) = (2°, -4°)$. Purple and orange dots represent AA stacking of the top and bottom pairs of adjacent layers, respectively. Together they form a supermoiré pattern with a unit cell outlined by a grey diamond. Blue, cyan, and magenta circles mark high-symmetry points of the supermoiré unit cell, where the shifts between two moiré AA stacking sites are **0**, ***β***, and ***δ***, respectively. **c-e**, Zoomed-in views of the moiré patterns at the three points marked in **b**. Black diamonds outline the moiré unit cells under the periodic approximation. **f-i**, Non-interacting band structures for different configurations along the magic continuum: $\theta_{12} : \theta_{23} = 1 : 2$ (**f**), $1 : -2$ (**g**), $1 : -3$ (**h**), and $1 : 3$ (**i**). These calculations are performed with zero interlayer electric potential difference. Local moiré band structures at the various high-symmetry points within the supermoiré unit cell are shown; each is coloured to match its corresponding panel in **c-e**.

tinuous lines in the parameter space exhibit either superconductivity or AHE. This fact, together with the physical expectation that the electronic structure varies smoothly with twist angles, strongly suggests that correlated phases in TTG are not restricted to isolated magic points but persist along an extended manifold, which we refer to as "magic continuum".

ELECTRONIC STRUCTURE OF MULTI-MOIRÉ TTG

Due to the lack of moiré commensuration, a global moiré band structure does not exist for multi-moiré TTG. Nonetheless, its electronic properties can be effectively modelled as spatially varying local moiré bands by approximating the structure as locally periodic on the moiré length scale. This is implemented by approximating the two twist angles as a fraction, $(\theta_{12}, \theta_{23}) \approx (p\theta_0, q\theta_0)$ with p and q being coprime integers, and applying a small structural distortion to render the two bilayer moiré wave vectors commensurate [3, 4]. Within this framework, a generalized Bistritzer–MacDonald continuum model [15] can be applied locally within each moiré unit cell of size $l_\mathrm{m} \approx a_0/\theta_0$, where $a_0 = 0.246\,\mathrm{nm}$ is the graphene lattice constant. The resulting local moiré bands are parametrized by the relative lateral displacement $\mathbf{d}$ between the two moiré lattices, which varies smoothly and periodically over the supermoiré (moiré of moiré) scale, $l_\mathrm{sm} \approx 2a_0/\left|(p+q)pq\theta_0^2\right|$. Figure **1b** illustrates the unrelaxed structure of multi-moiré TTG for $(\theta_{12}, \theta_{23}) = (2°, -4°)$, with the supermoiré unit cell outlined in gray. Figures **1c-e** show the approximated moiré unit cell at three high-symmetry points within the supermoiré unit cell (indicated by coloured circles in Fig. **1b**), with $\mathbf{d}$ labelled as $\mathbf{0}$, $\boldsymbol{\beta}$, and $\boldsymbol{\delta}$, respectively. These distinct moiré patterns exhibit different symmetries depending on $\mathbf{d}$ [16], and lead to a supermoiré-modulated local electronic structure. This is illustrated in Figs. **1f-i**, which present calculated non-interacting moiré band structures at the aforementioned $\mathbf{d}$ (indicated by different colours), for simple (p, q) of $(1, 2)$ (**f**), $(1, -2)$ (**g**), $(1, -3)$ (**h**), and $(1, 3)$ (**i**) (Methods H).

By maximizing the peak in the density of states averaged over different $\mathbf{d}$ values, one can determine a magic angle for each (p, q) combination, presenting target heterostructures likely to host correlated phases. Within the $(\theta_{12}, \theta_{23})$ parameter space, these magic angles for various (p, q) ratios lie along two branches of a magic continuum that extend through the alternating and helical twist quadrants, as shown in Fig. **1a** [2–5]. Exchanging θ_{12} and θ_{23} ($-\theta_{23}$) yields equivalent helical (alternating) structures. Therefore, the helical and alternating branches of the magic continuum are mirror symmetric about the lines $\theta_{12} = \theta_{23}$ and $\theta_{12} = -\theta_{23}$, respectively. In the following, we assume $|\theta_{23}/\theta_{12}| \geq 1$ without loss of generality. Notably, the two branches are not mirror images of each other about the $\theta_{23} = 0$ axis. For instance, the magic angle for $\theta_{12} = \theta_{23}$ is around 1.8°, whereas for $\theta_{12} = -\theta_{23}$, it is around 1.6°.

As either $|\theta_{12}|$ or $|\theta_{23}|$ increases, both branches of the magic continuum asymptotically approach the limit of magic-angle twisted bilayer graphene stacked on an electronically decoupled monolayer [17] (green-shaded regions in Fig. **1a**), in which the local low-energy electronic properties have a vanishing dependence on $\mathbf{d}$ (note that the decoupled layer is still expected to affect the bilayer via screening). This reduced $\mathbf{d}$-dependence is evident when comparing the local moiré band structures for $|\theta_{23}/\theta_{12}| = 3$ (Figs. **1h,i**) with those for $|\theta_{23}/\theta_{12}| = 2$ (Figs. **1f,g**). Below, we focus on the four structures with $(|\theta_{23}/\theta_{12}| \approx 2, 3)$, in which the supermoiré modulation of the local electronic properties plays a more important role. Results from two additional samples with $|\theta_{23}| \approx 15°$ are summarized in Extended Data Fig. **2**, serving as examples in which the third layer is electronically decoupled (see Methods C for a description of the twist angle determination).

CORRELATIONS AND AHE IN TTG MOIRÉ POLYCRYSTALS

Lattice relaxation in TTG depends on the specific angular configuration and can strongly reshape the supermoiré landscape. When θ_{23}/θ_{12} is close to ±1 or 2, TTG is predicted to relax to moiré-periodic domains separated by sharp domain walls on the supermoiré scale, resembling the structure of a polycrystal [4] (orange-shaded regions in Fig. **1a**). While moiré polycrystals with $|\theta_{23}/\theta_{12}| \approx 1$ have been studied experimentally [6, 7, 13, 14], here we report the first investigation of a moiré polycrystal with $\theta_{23}/\theta_{12} \approx 2$.

Figure **2a** shows the longitudinal resistance R_{xx} measured at $B = 0$ and $T = 300\,\mathrm{mK}$ as a function of vertical displacement field, D, and number of electrons per moiré unit cell, ν_m. Here, B and T denote the perpendicular magnetic field and temperature, respectively. The moiré unit cell was defined in the previous section using the local periodic approximation. In devices where either $p = 1$ or $q = 1$, this unit cell coincides with that of the small-angle bilayer moiré lattice (see, for example, Figs. **1c-e**). The large R_{xx} peaks at $\nu_\mathrm{m} = \pm 4$ originate from the reduced density of states when the flat moiré bands are empty or full. Additional R_{xx} peaks appear at $\nu_\mathrm{m} = -1, -2$ and -3, indicating spin and valley degeneracy lifting, driven by electronic correlations. To search for topologically non-trivial phases, we first measured the anomalous Hall response, R_{yx}^AHE, at small B, as illustrated in Figs. **2b, c** (see Methods B for the measurement details). Pronounced values of $\left|R_{yx}^\mathrm{AHE}\right|$ near $\nu_\mathrm{m} = \pm 1$ and ± 3 signal AHE, corroborated by field sweep measurements shown in Figs. **2d-g**. Hysteresis of the field-antisymmetrized Hall resistance, R_{yx}, around zero magnetic field reveals a ferromagnetic ground state (see Methods B for a description of the antisymmetrization procedure and Extended Data Fig. **3** for the raw data). The temperature dependence of R_{yx} curves near $\nu_\mathrm{m} = -1$

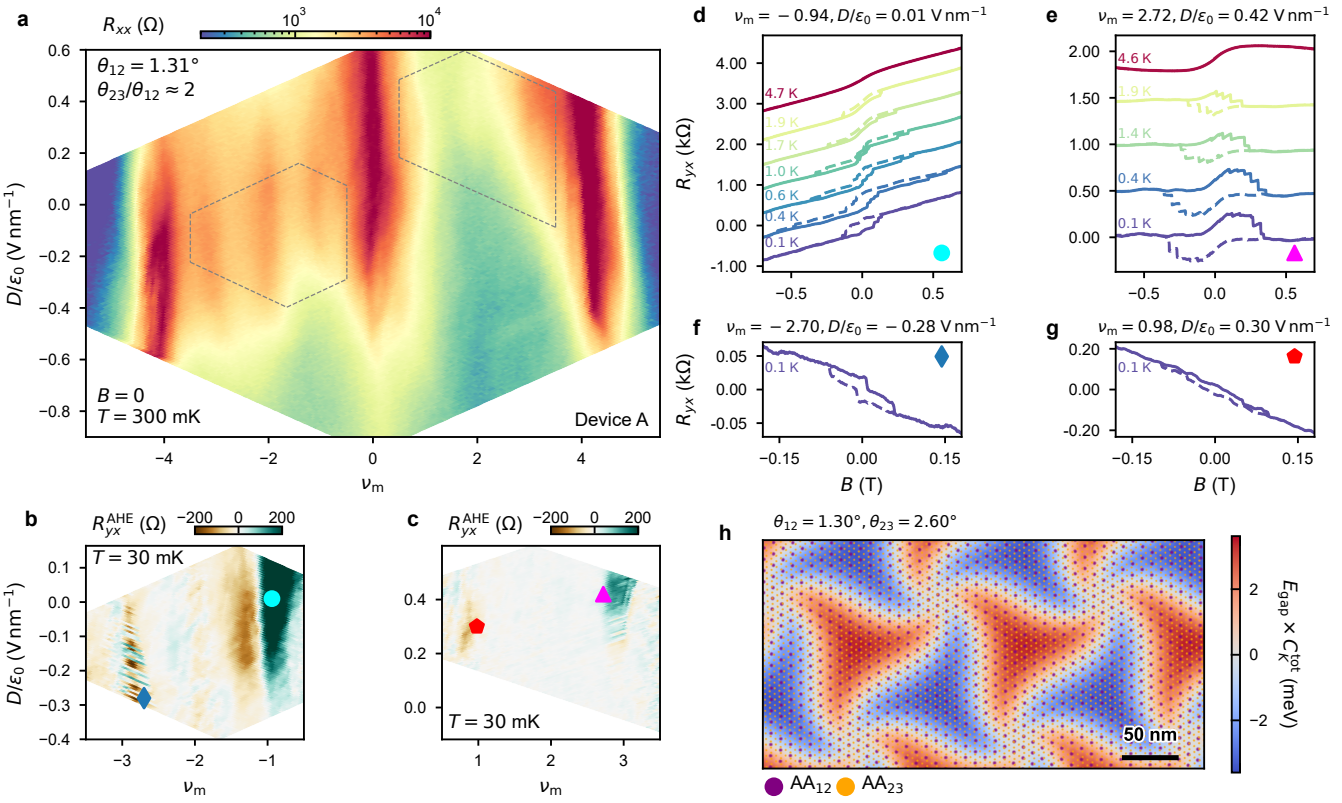

Fig. 2. Correlated states and AHE in polycrystalline TTG. a, R_{xx} versus ν_m and D measured at $B = 0$ and $T = 300$ mK for a moiré polycrystal TTG device with $\theta_{23}/\theta_{12} \approx 2$ (Device A), showing resistance peaks at charge neutrality ($\nu_m = 0$), at the full filling of the first moiré bands ($\nu_m = \pm 4$), and at correlated states ($\nu = -1, -2, -3$). **b,c**, R_{yx}^{AHE} (see Methods B) measured at $T = 30$ mK in hole- (**b**) and electron-doped (**c**) regions outlined by grey dashed polygons in **a**. Regions of large R_{yx}^{AHE} at $\nu_m = \pm 1, \pm 3$ indicate AHE. **d**, Field-antisymmetrized R_{yx} taken at $\nu_m = -0.94$ and $D/\epsilon_0 = 0.01$ V nm^{-1} (cyan circle in **b**) while sweeping B up (solid) and down (dashed) at different temperatures as indicated, demonstrating an AHE. Curves at different temperatures are shifted by 0.6 kΩ for clarity. **e**, Same as **d**, taken at $\nu_m = 2.72$, $D/\epsilon_0 = 0.42$ V nm^{-1} (pink triangle in **c**). Curves at different temperatures are shifted by 0.48 kΩ for clarity. **f**, Same as **d**, taken at $\nu_m = -2.70$, $D/\epsilon_0 = -0.28$ V nm^{-1}, $T = 0.1$ K (blue diamond in **b**). **g**, Same as **d**, taken at $\nu_m = 0.98$, $D/\epsilon_0 = 0.30$ V nm^{-1}, $T = 0.1$ K (red pentagon in **c**). **h**, Calculated supermoiré structure of TTG with $\theta_{12} = 1.30°, \theta_{23} = 2.60°$, including lattice relaxation. As in Fig. **1b**, purple and orange dots represent AA stacking of the top and bottom pairs of adjacent layers, respectively. Lattice relaxation leads to the formation of moiré periodic domains with $\mathbf{d} = \pm\boldsymbol{\delta}$ that host topological flat bands. Background colour represents $E_{gap} \times C_K^{tot}$ calculated for the local moiré lattices, where C_K^{tot} is the total Chern number per spin of the pair of flat bands in valley K, and $E_{gap} \geq 0$ is the minimum direct band gap at $\nu_m = \pm 4$. Red (blue) hues represent $C_K^{tot} = 1$ ($C_K^{tot} = -1$), whereas gray indicates gapless domain walls.

and 3 indicates a Curie temperature between 1.9 K and 4.6 K. Similar to other carbon-based materials, due to the weak spin-orbit coupling, the ferromagnetism observed here likely has an orbital origin [18, 19], a manifestation of non-zero Berry curvature.

Zero-field topological bands have not been observed in single-moiré 2D systems with global xy-inversion (C_{2z}) symmetry. In contrast, despite the global C_{2z} symmetry of our system, the multi-moiré structure combined with the aforementioned lattice relaxation leads to mesoscopic domains with uniform $\mathbf{d} = \pm\boldsymbol{\delta}$, which locally break C_{2z} symmetry (see Fig. **2h** for the relaxed structure calculated using the method of ref. [20–22]). This behaviour is analogous to helical trilayer graphene with $\theta_{12} \approx \theta_{23}$ [6]. Indeed, our band structure calculations produce nearly flat moiré bands with non-zero valley Chern numbers within each domain (Fig. **1f**, magenta). The observed AHE around odd integer fillings indicates spontaneous time-reversal symmetry breaking, likely originating from interaction-driven valley polarization or imbalance. Since neighbouring supermoiré domains are related by a C_{2z} operation, their local moiré flat bands possess opposite valley Chern numbers. When globally polarizing to the same valley, this results in a "Chern mosaic" (see Fig. **2h**) [23–25]. These Chern domains are separated by topologically protected gapless domain walls, consistent with the absence of quantized AHE in the experiment. We note that while the size and shape of the domains are extremely susceptible to strain and twist angle disorder [7], the band topology is expected to be robust.

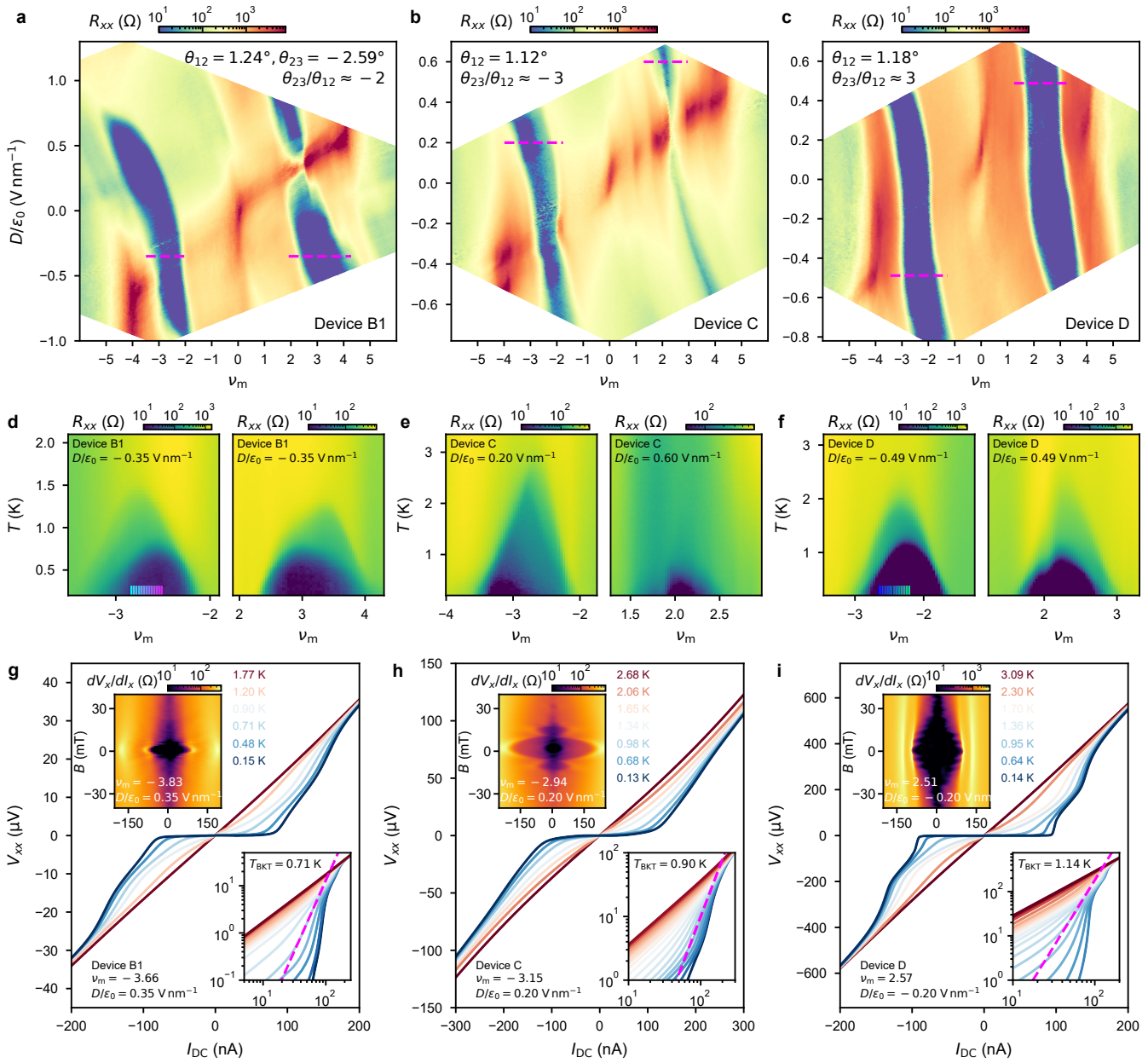

Fig. 3. Correlated states and robust superconductivity in quasicrystalline TTG. a-c, R_{xx} versus ν_m and D measured for devices with $\theta_{12} : \theta_{23} \approx 1 : -2$ (Device B1, **a**), $\theta_{12} : \theta_{23} \approx 1 : -3$ (Device C, **b**), and $\theta_{12} : \theta_{23} \approx 1 : 3$ (Device D, **c**), showing resistance peaks at charge neutrality ($\nu_m = 0$), at the full filling of the first moiré bands ($\nu_m = \pm 4$), and various correlated states at integer and fractional fillings. Blue regions indicate superconductivity. All data was taken at $B = 0$ and $T \approx 100$ mK. **d-f**, R_{xx} versus ν_m and T measured for Device B1 (**d**), Device C (**e**), and Device D (**f**), along the magenta lines marked in **a-c** (D values indicated in **d-f**), demonstrating superconducting transitions for all three quasicrystalline TTG devices on both electron- and hole-doped sides with critical temperatures on the order of 1 K. **g-i**, V_{xx} versus I_{DC} curves at various T, for the corresponding devices in **a-c**. ν_m and D values are indicated. Bottom-right insets show the same data in log-log scale, sampled at finer temperature increments. By fitting to $V_{xx} \propto I_{DC}^3$ (dashed magenta lines), we extract $T_{BKT} = 0.71\,\text{K}, 0.90\,\text{K}$, and 1.14 K for the three devices, respectively. Top-left insets show differential resistance dV_x/dI_x versus I_{DC} and small B, demonstrating Josephson interference patterns—evidence for phase coherent transport.

CORRELATIONS AND SUPERCONDUCTIVITY IN TTG MOIRÉ QUASICRYSTALS

When θ_{23}/θ_{12} is away from ±1 and 2, lattice relaxation is expected to have minimal impact on the supermoiré landscape, i.e., **d** evolves smoothly. The resulting structure has been referred to as a "moiré quasicrystal" [8] due to the incommensuration between the two moiré lattices.

Here, we present a systematic study of quasicrystalline TTG along both helical and alternating branches of the

magic continuum, showing results from devices close to simple angle ratios $\theta_{23}/\theta_{12} = -2, -3$ and 3. Figures **3a-c** show R_{xx} versus ν_m and D measured at $B = 0$ and $T = 100\,\mathrm{mK}$. Remarkably, all three structures demonstrate superconductivity, indicated by the deep blue areas. In addition to superconductivity, a series of correlated states at integer and fractional fillings manifests as peaks in R_{xx}, as summarized in Extended Data Table **1** (see Extended Data Fig. **4** and Methods D for correlated states under finite magnetic field). Local dispersive moiré bands coexist with local flat bands in quasicrystalline TTG (Figs. **1g-i**), allowing the former to shunt high-resistance correlated states supported by the latter. As a result, high-resistance states are prominent only along a diagonal line, where the Fermi level aligns with a low density of states in the local dispersive bands. In Device D (shown in Fig. **3c**), correlated high-resistance states are weak or absent, which may result from competition with superconductivity. Extended Data Figure **5** shows the same measurement performed at elevated temperature, where the correlated states become clearly resolved. Identifying the spin, valley, and sublattice order of different correlated states remains an open question for future theoretical and experimental studies. The many-body ground states are likely spatially modulated within the supermoiré unit cell due to the **d**-dependent moiré band structure, making local probes such as scanning tunnelling microscopy well-suited for this task [26, 27].

To further explore the superconducting properties of quasicrystalline TTG, we measured R_{xx} versus ν_m and T at constant D, showing characteristic superconducting domes with transition temperatures T_c around 1 K (Figs. **3d-f**). Figures **3g-i** present the DC voltage-current (V_{xx}–I_{DC}) characteristics at selected values of ν_m and D as a function of temperature. As T decreases, the V_{xx}–I_{DC} curves evolve from a linear (Ohmic) regime to a non-linear profile, characteristic of superconductivity. By fitting to $V_{xx} \propto I_{DC}^3$, we extract the Berezinskii–Kosterlitz–Thouless transition temperature, T_{BKT}, as shown in the bottom-right insets of Figs. **3g-i**. Furthermore, V_{xx}–I_{DC} measurements under a small perpendicular magnetic field reveal Fraunhofer-like interference patterns (Figs. **3g-i**, top-left insets), providing compelling evidence for the presence of phase-coherent superconductivity.

SIGNATURES FOR SUPERMOIRÉ-MODULATED SUPERCONDUCTIVITY

In Devices B1 and D, the superconducting regions exhibit a two-dome structure as a function of ν_m and T, shown in Figs. **3d,f**. This behaviour is further substantiated by the $R_{xx}(T)$ traces in Figs. **4a,b**, which exhibit two distinct transition temperatures where the resistance sharply drops upon cooling. Notably, this two-dome behaviour is a ubiquitous feature for devices

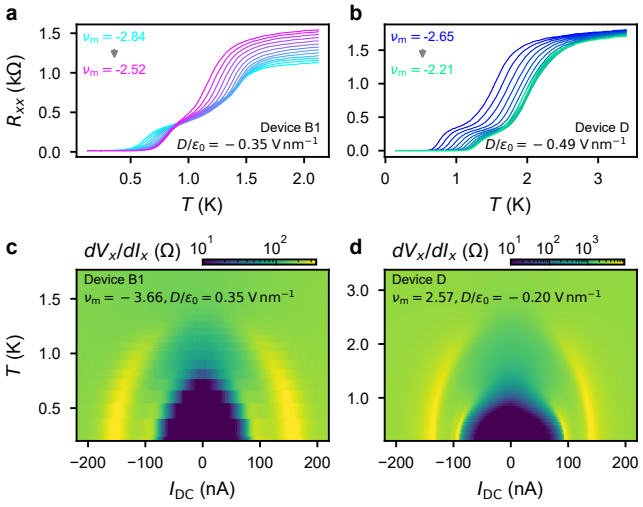

Fig. 4. Signatures for supermoiré-modulated superconductivity in quasicrystalline TTG. a-b, R_{xx} versus T measured in Device B1 (**a**) and Device D (**b**), both demonstrating a two-step behaviour of the superconducting transition. Curve colours in **a** (**b**) match the tick colours at the bottom of Fig. **3d** left (Fig. **3f** left), indicating ν_m and D where the data was taken. **c**, dV_x/dI_x versus I_{DC} and T measured in Device B1 (ν_m and D values are indicated). **d**, Same as **c**, measured in Device D. For both devices, two superconducting coherence peaks appear below the two superconducting transition temperatures, respectively. Non-linear resistance with coherence peaks indicates the existence of Cooper pairs in the intermediate temperature regime between the two transitions.

with $\theta_{23}/\theta_{12} \approx -2$ and 3 (see Extended Data Fig. **6** for more results from Devices B1, B2, and D), strongly indicating that it is intrinsic to the system rather than arising from extrinsic factors such as disorder. Between the two transitions, $R_{xx}(T)$ traces can be well described by the superconducting proximity effect model (Methods E and Extended Data Fig. **7**) [28], suggesting the existence of superconductor-normal metal-superconductor junctions. Furthermore, we measured differential resistance dV_x/dI_x as a function of I_{DC} and T (shown in Figs. **4c,d** and Extended Data Fig. **8**) and magnetoresistance $R_{xx}(B)$ as a function of T (shown in Extended Data Fig. **9**), both of which indicate that part of the sample remains superconducting between the two transition temperatures (see detailed discussion in Methods E).

Similar transport behaviour was reported in 2D systems with patterned superconducting islands [28–32], where the higher transition signals the onset of superconductivity within each island, and the lower transition corresponds to the establishment of global phase coherence across islands. A highly likely explanation of our results is that the superconductivity in these devices is spatially modulated on the supermoiré length scale, naturally originating from the **d**-dependent local electronic structure (see schematic in Extended Data Fig. **10**). At the higher transition temperature, certain regions within

the supermoiré unit cell—such as the area near $\mathbf{d} = \mathbf{0}$ in the schematic—become superconducting, resulting in a sharp drop in R_{xx}. Upon further cooling, two scenarios may occur at the lower transition temperature: (1) Josephson coupling between isolated superconducting regions becomes sufficiently strong to establish global phase coherence; or (2) the superconducting regions expand and form a percolating network of intrinsic superconductors. In both cases, these developments lead to a vanishing R_{xx}. Further discussion of this physical picture is provided in Methods E.

OUTLOOK

Single moiré twisted graphene systems can be divided into two families: alternating twisted graphene [9, 10, 13, 14, 33–35] (including twisted bilayer graphene) and twisted M+N-layer graphene [36–39] (M, N, or both are larger than 1). Although correlated states emerge in both families when the interlayer twist angles are appropriate, robust superconductivity has thus far been observed only in the former [10, 13, 14, 33–35], whereas the latter is typically characterized by Chern bands and usually exhibits the AHE [38, 39]. While non-trivial band topology is enabled by the absence of C_{2z} symmetry, the underlying conditions for superconductivity in moiré graphene systems require more investigation. Our systematic study of TTG indicates a phenomenological trend along the magic continuum: helically twisted moiré polycrystals, dominated by regions with $\mathbf{d} = \pm\boldsymbol{\delta}$, consistently host AHE, whereas robust superconductivity emerges in TTG moiré quasicrystals, where $\mathbf{d}$ varies smoothly across the supermoiré unit cell. This observation suggests that superconductivity is suppressed in regions where $\mathbf{d} = \pm\boldsymbol{\delta}$, despite the presence of local flat moiré bands. Thus, a high density of states alone is insufficient to drive superconductivity in graphene moiré systems, suggesting that additional factors—such as local symmetries—play an important role.

Furthermore, our results reveal the profound effects of the supermoiré. It gives rise to AHE in globally-C_{2z}-symmetric moiré polycrystals and modulates superconductivity in moiré quasicrystals. The latter, in particular, provides a new platform for studying the quantum breakdown of superconductivity [40]. While previous studies have constructed proximity-coupled arrays of superconducting islands to probe such transitions, moiré quasicrystals offer new opportunities due to several unique properties: (1) superconducting regions are naturally defined by atomically smooth, spatially varying moiré potentials rather than by lithographic patterning, (2) the characteristic size of superconducting regions is comparable to the superconducting coherence length, (3) the superconductivity is likely unconventional, as in other superconducting graphene moiré systems [41–46], and (4) regions with broken C_{2z} symmetry may host non-trivial local band topology that alters Josephson coupling. These features, combined with the exceptional tunability of 2D moiré materials, position moiré quasicrystals as a promising platform for exploring superconductor-metal transitions, anomalous metallic phases, and related emergent quantum phenomena.

Lastly, the concept of a magic continuum highlights that correlated phenomena are not confined to isolated "magic points," but can persist across extended regions—such as "magic hyperplanes"—in multi-dimensional parameter spaces spanned by continuous variables including multiple twist angles, strain, and pressure. This perspective offers a versatile route to exploring and engineering novel quantum phases [47–49]. With the advent of in-situ techniques capable of simultaneously tuning multiple degrees of freedom in 2D materials [50, 51], the landscape of accessible strongly correlated systems can be greatly expanded.

METHODS

A. Device fabrication

The van der Waals heterostructures were assembled in two parts using a standard dry-transfer technique [52]. First, a hexagonal boron nitride (hBN) flake (usually with a thickness of 15 nm - 30 nm) and a few-layer graphene strip were picked up by a poly(bisphenol A carbonate)/polydimethylsiloxane stamp. This bottom stack and poly(bisphenol A carbonate) film were released onto a 285 nm SiO_2/Si substrate. For devices with metallic bottom gates, only an hBN flake was picked up and released onto a pre-patterned metallic strip (15 nm Pd/Au alloy with a 2 nm Cr or Ti adhesion layer). After dissolving the poly(bisphenol A carbonate) film in chloroform, the bottom stack was annealed at 350 °C under vacuum for 12 hours to remove polymer residues. Then, tip cleaning was performed using the contact mode of an atomic force microscope to further clean the surface.

For assembling the twisted trilayer graphene, a monolayer graphene flake was cut into three pieces using an optical microscope with a fibre-coupled supercontinuum laser. A second poly(bisphenol A carbonate)/polydimethylsiloxane stamp was used to pick up an hBN flake and the three graphene pieces subsequently. Before the second and third pieces of graphene were picked up, the stage was rotated to realize the desired interlayer twist angle. Each layer of graphene was picked up slowly and at room temperature to minimize any unintentional perturbation of the twist angles. After assembling the top stack, it was released onto the bottom stack at 150 °C - 170 °C. This release step was done quickly to minimize the time spent at elevated temperatures.

The Hall bar was defined in a bubble-free region of the completed heterostructure, identified using atomic force microscopy. Patterns were defined using an Elionix ELS-HS50 electron-beam lithography system. A metallic top gate (25 nm - 65 nm Au with a 2 nm - 5 nm Cr or Ti adhesion layer) was deposited using a Sharon thermal evaporator. The device was connected using one-dimensional contacts (63 nm - 75 nm Au with a 2 nm - 5 nm Cr adhesion layer) [53]. Finally, the device was etched into a Hall bar geometry using reactive-ion etching.

B. Electrical transport measurements

Pre-characterization of the devices was carried out in a Janis helium-3 refrigerator with an 8 T perpendicular superconducting magnet and a base temperature of about 290 mK. A home-made 65 cm twisted-pair copper tape filter with ~ 20 MHz cut-off frequency [54] was thermally anchored at the helium-3 pot to prevent heating from Johnson noise and reduce the electron temperature. DC voltages were applied to the top and bottom gates using Keithley 2400/2450 source-measure units. The AC excitation of 1 nA – 10 nA at 10 Hz – 25 Hz was applied using Stanford Research Systems SR830 or SR860 lock-in amplifiers. The corresponding AC currents and voltages were preamplified by DL-1211 current preamplifiers and DL-1201/SR560 voltage preamplifiers respectively, then measured by the lock-in amplifiers. The temperature was measured using a calibrated CX-1010-CU-HT-0.1L thermometer.

A portion of the dilution refrigerator measurements were performed in a Bluefors LD250 using an Attocube two-way rotation probe. Two filters are installed and thermally anchored to the mixing chamber stage to reduce the electron temperature: a Quantum Machines Qfilter with a 65 kHz RC circuit and a 225 MHz LC circuit, and a home-made twisted-pair copper tape filter similar to the one mentioned above. Basel Precision Instruments SP983c-IF current preamplifiers and SP1004 voltage preamplifiers were used to achieve lower measurement noise. A Yokogawa GS210 was used to apply DC currents to devices through a 10 MΩ bias resistor. Other electronic instruments used in dilution refrigerator measurements are the same as those used in device pre-characterization. The temperature was measured using a calibrated RX-102A thermometer mounted on the sample probe. The temperature was controlled using a probe heater mounted close to both the thermometer and the thermal anchors of the wires, to guarantee good thermal connection among devices, the thermometer, and the heater.

The remaining dilution refrigerator measurements were performed in a wet Oxford Kelvinox TLM dilution refrigerator. Thermocoax cables were used from room temperature to 4 K, followed by RC filters before connecting to the sample. DC voltages were applied to the top and bottom gates using Yokogawa 7651 voltage sources. The AC currents and voltages were preamplified by DL-1211 current preamplifiers and SR560 voltage preamplifiers respectively, then measured by SR830 lock-in amplifiers.

High magnetic field measurements (up to 18 T) were taken using SCM-1 dilution refrigerator at the National High Magnetic Field Laboratory, with an 18 T superconducting magnet and a base temperature of about 20 mK. A home-made 20 cm twisted-pair copper tape filter was installed and immersed in the helium-3/helium-4 mixture to facilitate thermalization and filter high-frequency Johnson noise. The aforementioned electronics were used in the measurements.

By controlling voltages applied to the top and bottom gates (V_{tg} and V_{bg}), the electron density, n, and the perpendicular electric displacement field, D, can be tuned independently, following relations: $n = (\epsilon_{BN}\epsilon_0/e)(V_{bg}/d_{bg} + V_{tg}/d_{tg})$ and $D = \pm(\epsilon_{BN}\epsilon_0/2)(V_{bg}/d_{bg} - V_{tg}/d_{tg})$. Here, $\epsilon_{BN} = 3$ is the relative dielectric constant of hBN, ϵ_0 is the

vacuum permittivity, e is the elementary charge, and d_{bg} (d_{tg}) is the thickness of the bottom (top) hBN. In this work, we defined D such that $D > 0$ corresponds to a displacement field oriented from the small twist angle moiré towards the large twist angle moiré.

To map the anomalous Hall response shown in Figs. **2b, c** and minimize the contribution from both the regular Hall effect and R_{xx} mixing due to anisotropy, we measured R_{yx} at $B = \pm 60\,\mathrm{mT}$ and $\pm 30\,\mathrm{mT}$. The anomalous Hall response R_{yx}^{AHE} is then calculated according to $R_{yx}^{\mathrm{AHE}} = (R_{yx}^{30\,\mathrm{mT}} - R_{yx}^{-30\,\mathrm{mT}}) - (R_{yx}^{60\,\mathrm{mT}} - R_{yx}^{-60\,\mathrm{mT}})/2$. This procedure removes the regular Hall component when its contribution to R_{yx} has a linear dependence on B, which is in general true for the small B considered here. For the field sweep measurements shown in Figs. **2d-g**, R_{yx} is antisymmetrized between curves of opposite sweep direction, so that $R_{yx} = (R_{yx}^{\mathrm{raw}\uparrow}(B) - R_{yx}^{\mathrm{raw}\downarrow}(-B))/2$ (see $R_{yx}^{\mathrm{raw}}(B)$ in Extended Data Fig. **3**). Here, the arrows indicate the sweep direction of B.

C. Twist angle determination

We extract the interlayer twist angles of TTG devices through the following procedure: (1) By fitting the Landau levels to the Středa formula with the corresponding Chern numbers as extracted according to the quantized values of R_{yx}, we can calibrate the top and bottom gate capacitances. (2) Using these capacitance values, the charge density corresponding to $\nu_{\mathrm{m}} = \pm 4$ can be identified using R_{xx} peaks at integer fillings and Landau levels emanating from the charge neutral point and the band extrema. (3) The smaller twist angle can be calculated: $n_{\nu=\pm 4} = \pm 8 \sin^2\theta_{12}/\sqrt{3}a_0^2 \approx \pm 8\theta_{12}^2/\sqrt{3}a_0^2$. The errors in θ_{12} depend on the uncertainty in the fits to R_{xx} peaks and Landau levels, which are less than 0.05° in general.

The determination of the larger angle, θ_{23}, is more challenging given that the breakdown voltage of the hBN dielectric usually does not allow us to access $\nu_{\pm 4}$ fillings for layers 2 and 3. Here, we comment on this issue for each device. For Device A, for which we targeted $\theta_{23}/\theta_{12} = 2$, the fact that the AHE is observed indicates that the system relaxes to moiré periodic domains with the local angle ratio being exactly 2 (see Fig. **2h**). When the global angle ratio deviates from 2, these domains are still expected to form with smaller sizes as long as the deviation is small [6]. Therefore, the physical properties of the system remain qualitatively the same regardless of the exact value of θ_{23}. For Device B1, for which we targeted $\theta_{23}/\theta_{12} = -2$, we are able to dope to 4 holes per moiré unit cell of layer 2 and 3 (see results with extended gate ranges in Extended Data Fig. **11**). From its density, we extract $|\theta_{23}| = 2.59^\circ$ for Device B1. The extracted ratio between the two twist angles is -2.09, close to the target value. For Device B2, Device C, and Device D, we targeted ratios of $\theta_{23}/\theta_{12} = -2, -3$ and 3, respectively. The fact that we did not observe any R_{xx} peaks corresponding to the supermoiré density [55] sets an upper bound on the supermoiré density, and thus a lower bound on the supermoiré wavelength. From the width of the R_{xx} peak at charge neutrality, we estimate $l_{\mathrm{sm}}/l_{\mathrm{m}} \gtrsim 7$ for the devices studied here. From this estimated minimum l_{sm}, we can calculate the range of θ_{23} for each device, as shown in Extended Data Figs. **12c-e**. The resultant twist angle ratio ranges are $[-2.14, -1.86]$, $[-3.13, -2.87]$, and $[2.92, 3.07]$, for Device B2, Device C, and Device D, respectively. Although the exact values of θ_{23} are unknown for these devices, we argue that all discussions and conclusions presented in the paper are valid within the estimated θ_{23} ranges, since the main effect will be on the size of l_{sm} (see Methods F). For Device E and F, we targeted an interlayer twist between layers 2 and 3 of 15°. Within the possible error range, layer 3 will be electronically decoupled, representing the asymptotic limit of both branches of the magic continuum. Therefore, we argue that the exact value of θ_{23} is not important in these cases.

D. Correlated states of TTG moiré quasicrystals in finite magnetic fields

Extended Data Figure **4** shows Landau fan diagrams of our quasicrystalline TTG devices. Apart from quantum Hall states emanating from band edges and the charge neutrality point, the most prominent features that develop under an applied magnetic field exhibit Chern numbers $C = \pm 5, \pm 4, \pm 3$, as deduced from their Středa n-B slopes. These features extrapolate to a zero-field band fillings of $\nu_{\mathrm{m}} = \pm 1, \pm 2, \pm 3$, respectively. A similar sequence of correlated Chern insulators has been reported in magic-angle twisted bilayer graphene [56–66], the microscopic nature of which is likely the correlated Hofstadter ferromagnets [67].

E. Further discussion of supermoiré-modulated superconductivity

The superconducting proximity model [28] gives the following temperature dependence of R_{xx} between the two superconducting transitions, which we use to fit the experimental data:

$$R_{xx}(T) = R^0_{xx}\left(1 - A\xi_n \ln\left(\frac{B\xi_n(1-T/T_c)^2}{T}\right)\right). \quad (1)$$

Here, R^0_{xx} is the sample resistance after the islands become superconducting but before the proximity effect begins to reduce the resistance, T_c is the superconducting transition temperature of the islands, and ξ_n is the normal metal coherence length. Here, we neglect the temperature dependence of ξ_n and treat it as a fitting parameter, same as A and B. The fitting results are shown in Extended Data Fig. **7**. This model does not consider the BKT phase transition and therefore is not a meaningful fit of the experimental data below the lower transition. The extracted values of T_c match the higher transition temperatures of $R_{xx}(T)$ traces.

To better understand the nature of the two transitions, we measured differential resistance dV_x/dI_x as a function of I_{DC} and T, shown in Figs. **4c,d** and Extended Data Fig. **8**. At base temperature, two critical currents can be identified as peaks of dV_x/dI_x. Between them, non-zero dV_x/dI_x is observed that is consistent with the flux-flow regime of the Josephson junction array [68]. This phase evolves towards lower I_{DC} with increasing temperature and exists at $I_{DC} = 0$ between the two transition temperatures, suggesting that part of the sample remains superconducting in this temperature range. This conclusion is corroborated by the measurements of $R_{xx}(B)$ at different T, shown in Extended Data Fig. **9**. At temperatures above the higher transition, the increase of R_{xx} is proportional to B^2, as expected from the Drude model [69]. At temperatures between the two transitions, we observe a linear magnetoresistance at small B, consistent with the behaviour of Josephson junction arrays at small vortex densities [70].

For supermoiré-modulated superconductivity to emerge, two conditions must be satisfied: (1) $l_m \ll l_{sm}$ so that the supermoiré potential can be viewed as a slow modulation of a local electronic structure, and (2) $\xi_{GL} \lesssim l_{SC} < l_{sm}$ so that superconductivity can be established within certain regions in the supermoiré unit cell. Here, ξ_{GL} is the Ginzburg-Landau coherence length, and l_{SC} is the size of the superconducting islands between two transitions. The first condition is supported by the absence of R_{xx} peaks at the supermoiré density [55], from which we estimate $l_{sm}/l_m \gtrsim 7$ for the devices studied here as discussed in Methods C. To verify the second condition, we compare the l_{sm} and ξ_{GL} that we extract from the dependence of R_{xx} on B and T (see Extended Data Fig. **12**, Methods F, and Methods G). ξ_{GL} is about 15 nm – 50 nm across different devices, less than the expected supermoiré wavelength, $l_{sm} \gtrsim 100$ nm, for devices with $\theta_{23}/\theta_{12} \approx -2$ or 3.

It is worth noting that we did not observe oscillations of R_{xx} when the number of flux quanta per supermoiré unit cell is an integer or a simple fraction, as reported in other Josephson junction array systems [32, 71]. Possible reasons include considerable supermoiré disorder arising from twist angle variations and strain, as well as finite size effects. Future investigations will benefit from advances in fabrication techniques that minimize supermoiré disorder, as well as from scanning probes with moiré- or atomic-scale spatial resolution, which are essential for further studying the effects of supermoiré on superconductivity. In Device C, where $\theta_{23}/\theta_{12} \approx -3$, the signatures of supermoiré-modulated superconductivity are weak or absent within the superconducting phase space. This could originate from the weaker **d**-dependence of the local electronic structure, as illustrated in Fig. **1h**, suggesting that the third graphene layer is weakly coupled in this system.

F. Supermoiré wavelength calculations

When the ratio between the two twist angles of a TTG heterostructure is close to a simple fraction, i.e., $\theta_{12}/\theta_{23} \approx p/q$ with p and q being small coprime integers, the resulting structure can be understood approximately in terms of a commensurate moiré unit cell (consisting of $p\times p$ and $q\times q$ bilayer moiré unit cells defined by θ_{12} and θ_{23}, respectively), but with the offset between the two moiré patterns varying slowly at a supermoiré length scale given by

$$l_{sm} = \frac{a_0}{\sqrt{2q^2(1-\cos\theta_{12}) + 2p^2(1-\cos\theta_{23}) - 4|pq|\cos\left(\frac{\theta_{12}+\theta_{23}}{2}\right)\sqrt{(1-\cos\theta_{12})(1-\cos\theta_{23})}}}. \quad (2)$$

When both $|\theta_{12}|$ and $|\theta_{23}|$ are small and $\theta_{12}/\theta_{23} = p/q$, this equation can be approximated as $l_{sm} \approx 2a_0/|(p+q)\theta_{12}\theta_{23}|$. In practice, we calculate l_{sm} for arbitrary twist angle combinations by evaluating Eq. 2 for $1 \le |p|, |q| \le 10$ and choosing the largest resulting value (Extended Data Figs. **12a, b**).

G. Extraction of ξ_{GL}

To extract ξ_{GL}, we analyse the magnetic field dependence of the superconducting transition temperature. For each magnetic field, the $R_{xx}(T)$ trace above the higher transition is first fitted with a linear function of T to approximate the normal-state resistance. The superconducting transition temperature T_c is then defined as the temperature at which the measured resistance curve intersects 85%, 90%, or 95% of the fitted curve. The extracted T_c values are fitted as a linear function of B, following the Ginzburg-Landau relation:

$$\frac{T_c}{T_c^0} = 1 - \frac{2\pi\xi_{\mathrm{GL}}^2}{\Phi_0} B, \tag{3}$$

where $\Phi_0 = h/2e$ is the superconducting flux quantum, and T_c^0 is the zero-field superconducting transition temperature. The slope of the linear fit determines ξ_{GL}. While ξ_{GL} values extracted using different resistance thresholds (85%, 90%, 95%) differ slightly, they exhibit consistent trends as a function of ν_{m}. In Extended Data Fig. **12**, we plot the 90% criterion value of ξ_{GL} as the data point, with the range defined by the 85% and 95% criteria shown as error bars. Since the extraction is based on the field dependence of the higher transition, the obtained coherence length characterizes the superconducting regions that exist between the two transitions.

H. Electronic structure calculations

In this section, we describe the electronic band structure calculation of $\theta_{12}/\theta_{23} \approx p/q$ TTG shown in Fig. **1**, which are calculated using a continuum model for a commensurate p/q moiré supercell.

We start with the atomic lattice vectors for each graphene layer, given by the columns of the matrix $\boldsymbol{A}_\ell = \boldsymbol{R}(\theta_\ell)\boldsymbol{A}_0$, where $\ell = 1, 2, 3$ labels the layer index, $(\theta_1, \theta_2, \theta_3) = (-p\theta_0, 0, q\theta_0)$ are the twist angles of the three layers, and

$$\boldsymbol{R}(\theta) = \begin{pmatrix} \cos\theta & -\sin\theta \\ \sin\theta & \cos\theta \end{pmatrix}; \quad \boldsymbol{A}_0 = a_0 \begin{pmatrix} 1 & \frac{1}{2} \\ 0 & \frac{\sqrt{3}}{2} \end{pmatrix} \tag{4}$$

with $a_0 = 0.246\,\mathrm{nm}$. The moiré superlattice vectors are given by the columns of the matrix $\boldsymbol{A}_{12} \equiv (\boldsymbol{A}_1^{-1} - \boldsymbol{A}_2^{-1})^{-1}$ and $\boldsymbol{A}_{23} \equiv (\boldsymbol{A}_2^{-1} - \boldsymbol{A}_3^{-1})^{-1}$. In general, these two moiré superlattices are incommensurate but, for small twist angles, are almost commensurate $p\boldsymbol{A}_{12} \approx q\boldsymbol{A}_{23}$.

To proceed, we construct a local periodic structure. We consider a slight distortion of the lattices, which we denote with a prime $\boldsymbol{A}'_\ell$, for which the moiré scale structure is exactly periodic. Specifically, we take $\boldsymbol{A}'_1 = \boldsymbol{A}_1$ and $\boldsymbol{A}'_3 = \boldsymbol{A}_3$ to be unchanged, but slightly deform the middle layer as

$$\boldsymbol{A}_2 \to \boldsymbol{A}'_2 = \left(\frac{q}{p+q} \boldsymbol{A}_1^{-1} + \frac{p}{p+q} \boldsymbol{A}_3^{-1} \right)^{-1} \tag{5}$$

which results in the new moiré superlattice vectors satisfying

$$p\boldsymbol{A}'_{12} = q\boldsymbol{A}'_{23} = (p+q)\left(\boldsymbol{A}_1^{-1} - \boldsymbol{A}_3^{-1}\right)^{-1} \equiv \boldsymbol{A}_m \tag{6}$$

thus defining a commensurate moiré unit cell $\boldsymbol{A}_m$. To see that this is a small modification of the actual structure at small twist angles, notice that the deviation

$$\boldsymbol{A}'_2 - \boldsymbol{A}_2 = \frac{2pq}{p+q} i\theta_0 \sigma_y \boldsymbol{A}_0 + O(\theta_0^2) \tag{7}$$

is only non-zero at order θ_0 (in this analysis, we have assumed $p/q \neq -1$).

We can now calculate the local electronic properties. We consider three graphene sheets in the commensurate structure. Importantly, we allow each layer to be displaced in-plane according to a vector $\boldsymbol{s}_\ell$, such that the sublattice $\sigma \in \{A, B\}$ carbon atoms in layer ℓ are positioned at $\boldsymbol{A}'_\ell[(n,m)^{\mathsf{T}} + \boldsymbol{t}_\sigma + \boldsymbol{s}_\ell]$, where $\boldsymbol{t}_A = 0$ and $\boldsymbol{t}_B = (2/3, 1/3)^{\mathsf{T}}$. This shift is important to capture the local stacking configurations of trilayer graphene, which leads to different electronic properties.

We model the electronic properties using the standard continuum model approach, which is valid at small twist angles. We work in the Hilbert space spanned by $\{|\boldsymbol{k}, \ell, \sigma\rangle\}$, where $\boldsymbol{k}$ is momentum, $\ell = 1, 2, 3$ is layer, and $\sigma = A, B$ is sublattice. Let $\boldsymbol{B}'_\ell = 2\pi(\boldsymbol{A}'_\ell)^{-\mathsf{T}}$. We take $\boldsymbol{k}$ to be near the $\boldsymbol{K} \equiv \boldsymbol{B}_0(2/3, 1/3)^{\mathsf{T}}$ point. The intralayer terms are given

by the standard Dirac equation near the $\boldsymbol{K}_\ell = \boldsymbol{B}'_\ell(2/3, 1/3)^\mathsf{T}$ point,

$$\langle \boldsymbol{k}, \ell, \sigma' | H | \boldsymbol{k}, \ell, \sigma \rangle = v_F \begin{pmatrix} 0 & e^{i\theta_\ell}[k_x - ik_y - (K_{\ell,x} - iK_{\ell,y})] \\ c.c. & 0 \end{pmatrix}_{\sigma'\sigma} \tag{8}$$

For the interlayer tunnelling terms, we keep the (most dominant) first harmonic terms. For adjacent layers $|\ell' - \ell| = 1$, the non-zero interlayer tunnelling matrix elements are given by

$$\langle \boldsymbol{k} + \boldsymbol{q}_n^{\ell'\ell}, \ell', \sigma' | H | \boldsymbol{k}, \ell, \sigma \rangle = T^{\ell'\ell}_{n\sigma'\sigma}(\boldsymbol{k}) \tag{9}$$

for $n = 0, 1, 2$, indexes the three tunnelling matrix elements that shift momentum by $\boldsymbol{q}_n^{\ell'\ell} = (\boldsymbol{B}'_{\ell'} - \boldsymbol{B}'_\ell)\boldsymbol{z}_n$, with $\boldsymbol{z}_0 = (0,0)^\mathsf{T}$, $\boldsymbol{z}_1 = (-1,0)^\mathsf{T}$, $\boldsymbol{z}_2 = (-1,-1)^\mathsf{T}$. The matrix elements are given by

$$T^{\ell'\ell}_{n\sigma'\sigma}(\boldsymbol{k}) = we^{2\pi i \boldsymbol{z}_n \cdot (\boldsymbol{s}_\ell - \boldsymbol{s}_{\ell'})}(1 + \xi(|\boldsymbol{k} + \boldsymbol{B}_\ell \boldsymbol{z}_n| - |\boldsymbol{K}|)) \begin{pmatrix} 1 & \kappa e^{-2\pi i n/3} \\ \kappa e^{2\pi i n/3} & 1 \end{pmatrix}_{\sigma'\sigma} \tag{10}$$

There are a few differences in comparison to the standard Bistritzer-MacDonald for twisted bilayer graphene [15]. First, we explicitly take the in-plane displacements $\boldsymbol{s}_\ell$ into account via the phase factor $e^{2\pi i \boldsymbol{z}_n \cdot (\boldsymbol{s}_\ell - \boldsymbol{s}_{\ell'})}$. While for a bilayer, such a shift amounts to a redefinition of the origin, in the commensurate trilayer this shift is physical and impacts the electronic band structure. Second, we keep the first-order correction in the momentum dependence of the tunnelling term via the ξ term [6, 7, 72]. We use the parameters $v_F = 0.88 \times 10^6\ \mathrm{m\,s^{-1}}$, $w = 0.11\,\mathrm{eV}$, $\xi = -2.1\,\text{Å}$, and $\kappa = 0.68$.

In terms of the atomic displacements $\boldsymbol{s}_\ell$, the vector connecting the AA_{12} and AA_{23} sites in the commensurate structure is [4]

$$\boldsymbol{d} = \boldsymbol{A}_m \left(\frac{1}{p}(\boldsymbol{s}_1 - \boldsymbol{s}_2) - \frac{1}{q}(\boldsymbol{s}_2 - \boldsymbol{s}_3) \right) \tag{11}$$

The electronic structure only depends on $\boldsymbol{s}_\ell$ through $\boldsymbol{d}$ modulo $\frac{1}{|pq|}\boldsymbol{A}_m$. We take $\boldsymbol{s}_2 = \boldsymbol{s}_3 = (0,0)^\mathsf{T}$ and set $\boldsymbol{s}_1 = (0,0)^\mathsf{T}$ for the $\boldsymbol{d} = 0$ stacking, $\boldsymbol{s}_1 = \frac{1}{|q|}(1/3, 1/3)^\mathsf{T}$ for the $\boldsymbol{d} = \boldsymbol{\delta}$ stacking, and $\boldsymbol{s}_1 = \frac{1}{|q|}(1/2, 0)^\mathsf{T}$ for the $\boldsymbol{d} = \boldsymbol{\beta}$ stacking configurations.

ACKNOWLEDGEMENTS

We thank C. Yang for sharing unpublished calculation results. We thank B. Feldman for helpful feedback on the paper. We thank G. de la Fuente Simarro for assistance with device fabrication and transport measurements. We thank A. Bangura, G. Jones, R. Nowell, A. Woods, and S. Hannahs for supporting measurements performed at the National High Magnetic Field Laboratory. Work in the P.J.-H. group was partially supported by the Army Research Office MURI W911NF2120147, the Air Force Office of Scientific Research (AFOSR) grant FA9550-21-1-0319, the National Science Foundation (DMR-1809802), a Max Planck-Humboldt Research Award to P.J.-H., the CIFAR Quantum Materials Program, the Ramón Areces Foundation, and the Gordon and Betty Moore Foundation's EPiQS Initiative through grant GBMF9463 to P.J.-H. A.U. acknowledges support from the MIT Pappalardo Fellowship and from the VATAT Outstanding Postdoctoral Fellowship in Quantum Science and Technology. A.S. was supported by the US Department of Energy, Office of Science, Basic Energy Sciences, Materials Sciences and Engineering Division, under Contract DE-AC02-76SF00515. F.G. is grateful for the financial support from the Swiss National Science Foundation (Postdoc.Mobility Grant No. 222230). K.W. and T.T. acknowledge support from the JSPS KAKENHI (Grant Numbers 21H05233 and 23H02052) , the CREST (JPMJCR24A5), JST and World Premier International Research Center Initiative (WPI), MEXT, Japan. L.F. was supported primarily by Simons Investigator Award from Simons Foundation. T.D. was supported by a startup fund at Stanford University. J.H.S. acknowledges financial support from the German Science Foundation through the SPP2244 program. A portion of this work was performed at the National High Magnetic Field Laboratory, which is supported by National Science Foundation Cooperative Agreement No. DMR-2128556 and the State of Florida. This work was performed in part at the Harvard University Center for Nanoscale Systems (CNS); a member of the National Nanotechnology Coordinated Infrastructure Network (NNCI), which is supported by the National Science Foundation under NSF award no. ECCS-2025158. This work was carried out in part through the use of MIT.nano's facilities.

AUTHOR CONTRIBUTIONS

A.U., L.-Q.X., and P.J.-H. conceived the project. L.-Q.X. fabricated the devices with the help of A.U. L.-Q.X. carried out the helium-3 refrigerator measurements with the help of A.U., J.Y., and A.S. L.-Q.X. and A.U. carried out a portion of the dilution refrigerator measurements under the supervision of P.J.-H. J.Y. carried out the remaining dilution refrigerator measurements under the supervision of J.H.S. L.-Q.X. and A.S. carried out measurements at the National High Magnetic Field Laboratory. T.D., N.S.T., and J.M.-M. performed band structure and lattice relaxation calculations. K.W. and T.T. supplied the boron nitride crystals. L.-Q.X., A.U., J.Y., A.S., F.G., N.S.T., J.M.-M., T.D., L.F., and P.J.-H. analysed the data and discussed the interpretation. L.-Q.X. wrote the manuscript with the help of A.U. and A.S., and input from all authors. P.J.-H. supervised the project.

COMPETING INTERESTS

The authors declare no competing interests.

DATA AVAILABILITY

The data that support the findings of this study are available from the corresponding authors upon reasonable request.

[1] E. Y. Andrei, D. K. Efetov, P. Jarillo-Herrero, A. H. MacDonald, K. F. Mak, T. Senthil, E. Tutuc, A. Yazdani, and A. F. Young, The marvels of moiré materials, Nature Reviews Materials **6**, 201 (2021).

[2] Z. Zhu, S. Carr, D. Massatt, M. Luskin, and E. Kaxiras, Twisted trilayer graphene: A precisely tunable platform for correlated electrons, Phys. Rev. Lett. **125**, 116404 (2020).

[3] F. K. Popov and G. Tarnopolsky, Magic angle butterfly in twisted trilayer graphene, Phys. Rev. Res. **5**, 043079 (2023).

[4] C. Yang, J. May-Mann, Z. Zhu, and T. Devakul, Multi-moiré trilayer graphene: Lattice relaxation, electronic structure, and magic angles, Phys. Rev. B **110**, 115434 (2024).

[5] D. C. W. Foo, Z. Zhan, M. M. Al Ezzi, L. Peng, S. Adam, and F. Guinea, Extended magic phase in twisted graphene multilayers, Phys. Rev. Res. **6**, 013165 (2024).

[6] L.-Q. Xia, S. C. de la Barrera, A. Uri, A. Sharpe, Y. H. Kwan, Z. Zhu, K. Watanabe, T. Taniguchi, D. Goldhaber-Gordon, L. Fu, T. Devakul, and P. Jarillo-Herrero, Topological bands and correlated states in helical trilayer graphene, Nature Physics **21**, 239 (2025).

[7] J. C. Hoke, Y. Li, Y. Hu, J. May-Mann, K. Watanabe, T. Taniguchi, T. Devakul, and B. E. Feldman, Imaging supermoire relaxation and conductive domain walls in helical trilayer graphene (2024), arXiv:2410.16269 [cond-mat.mes-hall].

[8] A. Uri, S. C. de la Barrera, M. T. Randeria, D. Rodan-Legrain, T. Devakul, P. J. D. Crowley, N. Paul, K. Watanabe, T. Taniguchi, R. Lifshitz, L. Fu, R. C. Ashoori, and P. Jarillo-Herrero, Superconductivity and strong interactions in a tunable moiré quasicrystal, Nature **620**, 762 (2023).

[9] Y. Cao, V. Fatemi, A. Demir, S. Fang, S. L. Tomarken, J. Y. Luo, J. D. Sanchez-Yamagishi, K. Watanabe, T. Taniguchi, E. Kaxiras, R. C. Ashoori, and P. Jarillo-Herrero, Correlated insulator behaviour at half-filling in magic-angle graphene superlattices, Nature **556**, 80 (2018).

[10] Y. Cao, V. Fatemi, S. Fang, K. Watanabe, T. Taniguchi, E. Kaxiras, and P. Jarillo-Herrero, Unconventional superconductivity in magic-angle graphene superlattices, Nature **556**, 43 (2018).

[11] M. Serlin, C. L. Tschirhart, H. Polshyn, Y. Zhang, J. Zhu, K. Watanabe, T. Taniguchi, L. Balents, and A. F. Young, Intrinsic quantized anomalous Hall effect in a moiré heterostructure, Science **367**, 900 (2020).

[12] H. Park, J. Cai, E. Anderson, Y. Zhang, J. Zhu, X. Liu, C. Wang, W. Holtzmann, C. Hu, Z. Liu, T. Taniguchi, K. Watanabe, J.-h. Chu, T. Cao, L. Fu, W. Yao, C.-Z. Chang, D. Cobden, D. Xiao, and X. Xu, Observation of fractionally quantized anomalous Hall effect, Nature **622**, 74 (2023).

[13] J. M. Park, Y. Cao, K. Watanabe, T. Taniguchi, and P. Jarillo-Herrero, Tunable strongly coupled superconductivity in magic-angle twisted trilayer graphene, Nature **590**, 249 (2021).

[14] Z. Hao, A. M. Zimmerman, P. Ledwith, E. Khalaf, D. H. Najafabadi, K. Watanabe, T. Taniguchi, A. Vishwanath, and P. Kim, Electric field–tunable superconductivity in alternating-twist magic-angle trilayer graphene, Science **371**, 1133 (2021).

[15] R. Bistritzer and A. H. MacDonald, Moiré bands in twisted double-layer graphene, Proceedings of the National Academy of Sciences **108**, 12233 (2011).

[16] C.-Y. Hao, Z. Zhan, P. A. Pantaleón, J.-Q. He, Y.-X. Zhao, K. Watanabe, T. Taniguchi, F. Guinea, and L. He, Robust flat bands in twisted trilayer graphene moiré quasicrystals, Nature Communications **15**, 8437 (2024).

[17] J. C. Hoke, Y. Li, J. May-Mann, K. Watanabe, T. Taniguchi, B. Bradlyn, T. L. Hughes, and B. E. Feldman, Uncovering the spin ordering in magic-angle graphene via edge state equilibration, Nature Communications **15**, 4321 (2024).

[18] C. L. Tschirhart, M. Serlin, H. Polshyn, A. Shragai, Z. Xia, J. Zhu, Y. Zhang, K. Watanabe, T. Taniguchi, M. E. Huber, and A. F. Young, Imaging orbital ferromagnetism in a moiré chern insulator, Science **372**, 1323 (2021).

[19] A. L. Sharpe, E. J. Fox, A. W. Barnard, J. Finney, K. Watanabe, T. Taniguchi, M. A. Kastner, and D. Goldhaber-Gordon, Evidence of orbital ferromagnetism in twisted bilayer graphene aligned to hexagonal boron nitride, Nano Letters **21**, 4299 (2021).

[20] S. Carr, D. Massatt, S. B. Torrisi, P. Cazeaux, M. Luskin, and E. Kaxiras, Relaxation and domain formation in incommensurate two-dimensional heterostructures, Phys. Rev. B **98**, 224102 (2018).

[21] P. Cazeaux, M. Luskin, and D. Massatt, Energy minimization of two dimensional incommensurate heterostructures, Archive for Rational Mechanics and Analysis **235**, 1289 (2019).

[22] Z. Zhu, P. Cazeaux, M. Luskin, and E. Kaxiras, Modeling mechanical relaxation in incommensurate trilayer van der waals heterostructures, Phys. Rev. B **101**, 224107 (2020).

[23] S. Grover, M. Bocarsly, A. Uri, P. Stepanov, G. Di Battista, I. Roy, J. Xiao, A. Y. Meltzer, Y. Myasoedov, K. Pareek, K. Watanabe, T. Taniguchi, B. Yan, A. Stern, E. Berg, D. K. Efetov, and E. Zeldov, Chern mosaic and berry-curvature magnetism in magic-angle graphene, Nature Physics **18**, 885 (2022).

[24] T. Devakul, P. J. Ledwith, L.-Q. Xia, A. Uri, S. C. de la Barrera, P. Jarillo-Herrero, and L. Fu, Magic-angle helical trilayer graphene, Science Advances **9**, eadi6063 (2023).

[25] D. Guerci, Y. Mao, and C. Mora, Chern mosaic and ideal flat bands in equal-twist trilayer graphene, Phys. Rev. Res. **6**, L022025 (2024).

[26] K. P. Nuckolls, R. L. Lee, M. Oh, D. Wong, T. Soejima, J. P. Hong, D. Călugăru, J. Herzog-Arbeitman, B. A. Bernevig, K. Watanabe, T. Taniguchi, N. Regnault, M. P. Zaletel, and A. Yazdani, Quantum textures of the many-body wavefunctions in magic-angle graphene, Nature **620**, 525 (2023).

[27] H. Kim, Y. Choi, É. Lantagne-Hurtubise, C. Lewandowski, A. Thomson, L. Kong, H. Zhou, E. Baum, Y. Zhang, L. Holleis, K. Watanabe, T. Taniguchi, A. F. Young, J. Alicea, and S. Nadj-Perge, Imaging inter-valley coherent order in magic-angle twisted trilayer graphene, Nature **623**, 942 (2023).

[28] D. W. Abraham, C. J. Lobb, M. Tinkham, and T. M. Klapwijk, Resistive transition in two-dimensional arrays of superconducting weak links, Phys. Rev. B **26**, 5268 (1982).

[29] D. J. Resnick, J. C. Garland, J. T. Boyd, S. Shoemaker, and R. S. Newrock, Kosterlitz-thouless transition in proximity-coupled superconducting arrays, Phys. Rev. Lett. **47**, 1542 (1981).

[30] S. Eley, S. Gopalakrishnan, P. M. Goldbart, and N. Mason, Approaching zero-temperature metallic states in mesoscopic superconductor–normal–superconductor arrays, Nature Physics **8**, 59 (2012).

[31] Z. Han, A. Allain, H. Arjmandi-Tash, K. Tikhonov, M. Feigel'man, B. Sacépé, and V. Bouchiat, Collapse of superconductivity in a hybrid tin–graphene josephson junction array, Nature Physics **10**, 380 (2014).

[32] C. G. L. Bøttcher, F. Nichele, M. Kjaergaard, H. J. Suominen, J. Shabani, C. J. Palmstrøm, and C. M. Marcus, Superconducting, insulating and anomalous metallic regimes in a gated two-dimensional semiconductor–superconductor array, Nature Physics **14**, 1138 (2018).

[33] J. M. Park, Y. Cao, L.-Q. Xia, S. Sun, K. Watanabe, T. Taniguchi, and P. Jarillo-Herrero, Robust superconductivity in magic-angle multilayer graphene family, Nature Materials **21**, 877 (2022).

[34] Y. Zhang, R. Polski, C. Lewandowski, A. Thomson, Y. Peng, Y. Choi, H. Kim, K. Watanabe, T. Taniguchi, J. Alicea, F. von Oppen, G. Refael, and S. Nadj-Perge, Promotion of superconductivity in magic-angle graphene multilayers, Science **377**, 1538 (2022).

[35] G. W. Burg, E. Khalaf, Y. Wang, K. Watanabe, T. Taniguchi, and E. Tutuc, Emergence of correlations in alternating twist quadrilayer graphene, Nature Materials **21**, 884 (2022).

[36] Y. Cao, D. Rodan-Legrain, O. Rubies-Bigorda, J. M. Park, K. Watanabe, T. Taniguchi, and P. Jarillo-Herrero, Tunable correlated states and spin-polarized phases in twisted bilayer–bilayer graphene, Nature **583**, 215 (2020).

[37] X. Liu, Z. Hao, E. Khalaf, J. Y. Lee, Y. Ronen, H. Yoo, D. Haei Najafabadi, K. Watanabe, T. Taniguchi, A. Vishwanath, and P. Kim, Tunable spin-polarized correlated states in twisted double bilayer graphene, Nature **583**, 221 (2020).

[38] H. Polshyn, J. Zhu, M. A. Kumar, Y. Zhang, F. Yang, C. L. Tschirhart, M. Serlin, K. Watanabe, T. Taniguchi, A. H. MacDonald, and A. F. Young, Electrical switching of magnetic order in an orbital Chern insulator, Nature **588**, 66 (2020).

[39] D. Waters, R. Su, E. Thompson, A. Okounkova, E. Arreguin-Martinez, M. He, K. Hinds, K. Watanabe, T. Taniguchi, X. Xu, Y.-H. Zhang, J. Folk, and M. Yankowitz, Topological flat bands in a family of multilayer graphene moiré lattices, Nature Communications **15**, 10552 (2024).

[40] B. Sacépé, M. Feigel'man, and T. M. Klapwijk, Quantum breakdown of superconductivity in low-dimensional materials, Nature Physics **16**, 734 (2020).

[41] Y. Cao, J. M. Park, K. Watanabe, T. Taniguchi, and P. Jarillo-Herrero, Pauli-limit violation and re-entrant superconductivity in moiré graphene, Nature **595**, 526 (2021).

[42] M. Oh, K. P. Nuckolls, D. Wong, R. L. Lee, X. Liu, K. Watanabe, T. Taniguchi, and A. Yazdani, Evidence for unconventional superconductivity in twisted bilayer graphene, Nature **600**, 240 (2021).

[43] H. Kim, Y. Choi, C. Lewandowski, A. Thomson, Y. Zhang, R. Polski, K. Watanabe, T. Taniguchi, J. Alicea, and S. Nadj-Perge, Evidence for unconventional superconductivity in twisted trilayer graphene, Nature **606**, 494 (2022).

[44] M. Tanaka, J. Î.-j. Wang, T. H. Dinh, D. Rodan-Legrain, S. Zaman, M. Hays, A. Almanakly, B. Kannan, D. K. Kim, B. M. Niedzielski, K. Serniak, M. E. Schwartz, K. Watanabe, T. Taniguchi, T. P. Orlando, S. Gustavsson, J. A. Grover, P. Jarillo-Herrero, and W. D. Oliver, Superfluid stiffness of magic-angle twisted bilayer graphene, Nature **638**, 99 (2025).

[45] A. Banerjee, Z. Hao, M. Kreidel, P. Ledwith, I. Phinney, J. M. Park, A. Zimmerman, M. E. Wesson, K. Watanabe, T. Taniguchi, R. M. Westervelt, A. Yacoby, P. Jarillo-Herrero, P. A. Volkov, A. Vishwanath, K. C. Fong, and P. Kim, Superfluid stiffness of twisted trilayer graphene superconductors, Nature **638**, 93 (2025).

[46] J. M. Park, S. Sun, K. Watanabe, T. Taniguchi, and P. Jarillo-Herrero, Simultaneous transport and tunneling spectroscopy of moiré graphene: Distinct observation of the superconducting gap and signatures of nodal superconductivity (2025), arXiv:2503.16410 [cond-mat.supr-con].

[47] S. Carr, S. Fang, P. Jarillo-Herrero, and E. Kaxiras, Pressure dependence of the magic twist angle in graphene superlattices, Phys. Rev. B **98**, 085144 (2018).

[48] M. Yankowitz, S. Chen, H. Polshyn, Y. Zhang, K. Watanabe, T. Taniguchi, D. Graf, A. F. Young, and C. R. Dean, Tuning superconductivity in twisted bilayer graphene, Science **363**, 1059 (2019).

[49] N. Morales-Durán, J. Wang, G. R. Schleder, M. Angeli, Z. Zhu, E. Kaxiras, C. Repellin, and J. Cano, Pressure-enhanced fractional chern insulators along a magic line in moiré transition metal dichalcogenides, Phys. Rev. Res. **5**, L032022 (2023).

[50] A. Inbar, J. Birkbeck, J. Xiao, T. Taniguchi, K. Watanabe, B. Yan, Y. Oreg, A. Stern, E. Berg, and S. Ilani, The quantum twisting microscope, Nature **614**, 682 (2023).

[51] H. Tang, Y. Wang, X. Ni, K. Watanabe, T. Taniguchi, P. Jarillo-Herrero, S. Fan, E. Mazur, A. Yacoby, and Y. Cao, On-chip multi-degree-of-freedom control of two-dimensional materials, Nature **632**, 1038 (2024).

[52] S. Sun and P. Jarillo-Herrero, Optimized fabrication procedure for high-quality graphene-based moiré superlattice devices, JoVE , e68230 (2025).

[53] L. Wang, I. Meric, P. Y. Huang, Q. Gao, Y. Gao, H. Tran, T. Taniguchi, K. Watanabe, L. M. Campos, D. A. Muller, J. Guo, P. Kim, J. Hone, K. L. Shepard, and C. R. Dean, One-dimensional electrical contact to a two-dimensional material, Science **342**, 614 (2013).

[54] L. Spietz, J. Teufel, and R. J. Schoelkopf, A twisted pair cryogenic filter (2006), arXiv:cond-mat/0601316 [cond-mat.other].

[55] Y. Xie, A. T. Pierce, J. M. Park, D. E. Parker, J. Wang, P. Ledwith, Z. Cai, K. Watanabe, T. Taniguchi, E. Khalaf, A. Vishwanath, P. Jarillo-Herrero, and A. Yacoby, Strong interactions and isospin symmetry breaking in a supermoiré lattice, Science **389**, 736 (2025).

[56] S. L. Tomarken, Y. Cao, A. Demir, K. Watanabe, T. Taniguchi, P. Jarillo-Herrero, and R. C. Ashoori, Electronic compressibility of magic-angle graphene superlattices, Phys. Rev. Lett. **123**, 046601 (2019).

[57] K. P. Nuckolls, M. Oh, D. Wong, B. Lian, K. Watanabe, T. Taniguchi, B. A. Bernevig, and A. Yazdani, Strongly correlated chern insulators in magic-angle twisted bilayer graphene, Nature **588**, 610 (2020).

[58] Y. Choi, H. Kim, Y. Peng, A. Thomson, C. Lewandowski, R. Polski, Y. Zhang, H. S. Arora, K. Watanabe, T. Taniguchi, J. Alicea, and S. Nadj-Perge, Correlation-driven topological phases in magic-angle twisted bilayer graphene, Nature **589**, 536 (2021).

[59] J. M. Park, Y. Cao, K. Watanabe, T. Taniguchi, and P. Jarillo-Herrero, Flavour hund's coupling, chern gaps and charge diffusivity in moiré graphene, Nature **592**, 43 (2021).

[60] S. Wu, Z. Zhang, K. Watanabe, T. Taniguchi, and E. Y. Andrei, Chern insulators, van hove singularities and topological flat bands in magic-angle twisted bilayer graphene, Nature Materials **20**, 488 (2021).

[61] Y. Saito, J. Ge, L. Rademaker, K. Watanabe, T. Taniguchi, D. A. Abanin, and A. F. Young, Hofstadter subband ferromagnetism and symmetry-broken chern insulators in twisted bilayer graphene, Nature Physics **17**, 478 (2021).

[62] I. Das, X. Lu, J. Herzog-Arbeitman, Z.-D. Song, K. Watanabe, T. Taniguchi, B. A. Bernevig, and D. K. Efetov, Symmetry-broken chern insulators and rashba-like landau-level crossings in magic-angle bilayer graphene, Nature Physics **17**, 710 (2021).

[63] P. Stepanov, M. Xie, T. Taniguchi, K. Watanabe, X. Lu, A. H. MacDonald, B. A. Bernevig, and D. K. Efetov, Competing zero-field chern insulators in superconducting twisted bilayer graphene, Phys. Rev. Lett. **127**, 197701 (2021).

[64] J. Yu, B. A. Foutty, Z. Han, M. E. Barber, Y. Schattner, K. Watanabe, T. Taniguchi, P. Phillips, Z.-X. Shen, S. A. Kivelson, and B. E. Feldman, Correlated hofstadter spectrum and flavour phase diagram in magic-angle twisted bilayer graphene, Nature Physics **18**, 825 (2022).

[65] M. He, X. Wang, J. Cai, J. Herzog-Arbeitman, R. Peng, T. Taniguchi, K. Watanabe, A. Stern, B. A. Bernevig, M. Yankowitz, O. Vafek, and X. Xu, Strongly interacting hofstadter states in magic-angle twisted bilayer graphene, Nature Physics 10.1038/s41567-025-02997-4 (2025).

[66] J. Finney, A. L. Sharpe, L. K. Rodenbach, J. Kang, X. Wang, K. Watanabe, T. Taniguchi, M. A. Kastner, O. Vafek, and D. Goldhaber-Gordon, Extended fractional chern insulators near half flux in twisted bilayer graphene above the magic angle (2025), arXiv:2503.12819 [cond-mat.mes-hall].

[67] X. Wang and O. Vafek, Theory of correlated chern insulators in twisted bilayer graphene, Phys. Rev. X **14**, 021042 (2024).

[68] T. P. Orlando, J. E. Mooij, and H. S. J. van der Zant, Phenomenological model of vortex dynamics in arrays of josephson junctions, Phys. Rev. B **43**, 10218 (1991).

[69] A. B. Pippard, *Magnetoresistance in metals*, Vol. 2 (Cambridge university press, 1989).

[70] M. S. Rzchowski, S. P. Benz, M. Tinkham, and C. J. Lobb, Vortex pinning in josephson-junction arrays, Phys. Rev. B **42**, 2041 (1990).

[71] M. Tinkham, D. W. Abraham, and C. J. Lobb, Periodic flux dependence of the resistive transition in two-dimensional superconducting arrays, Phys. Rev. B **28**, 6578 (1983).

[72] Y. H. Kwan, T. Tan, and T. Devakul, Fractional chern mosaic in supermoiré graphene (2024), arXiv:2411.08880 [cond-mat.str-el].

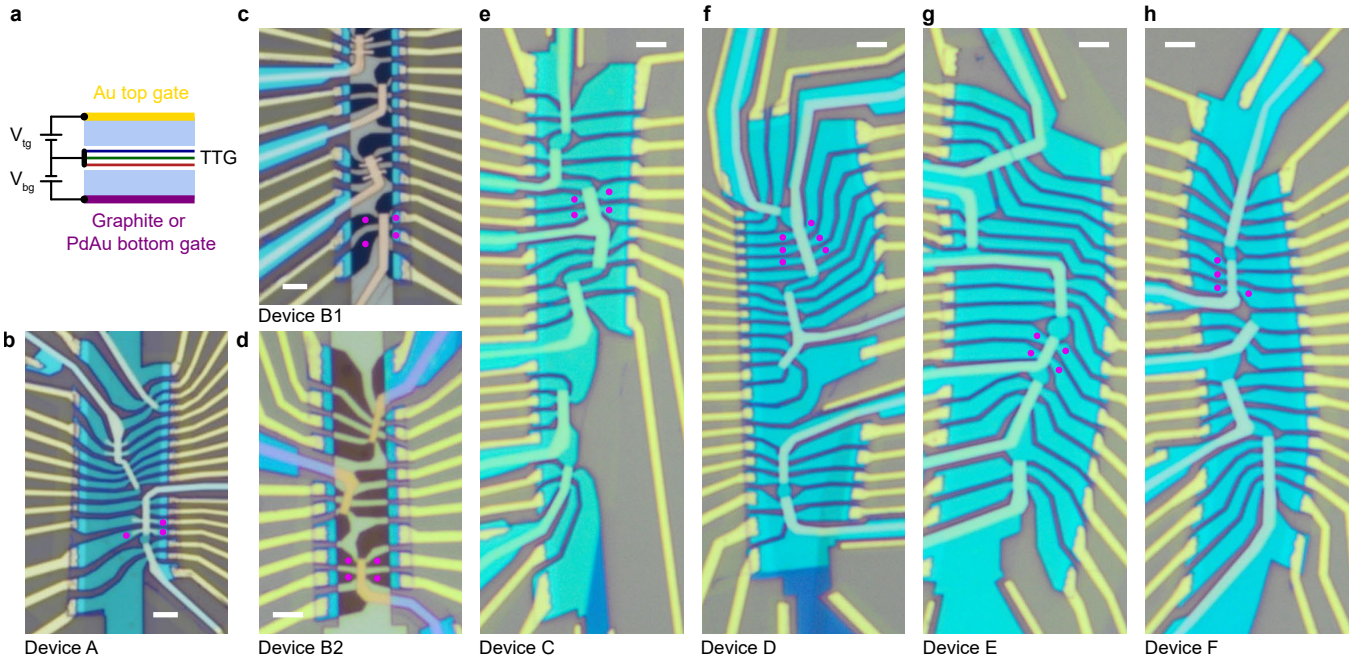

Extended Data Fig. 1. Circuit diagram and optical micrographs of TTG devices. **a**, Circuit diagram of TTG surrounded by two hBN dielectric layers and top and bottom gate electrodes (Au top gate and graphite or PdAu bottom gate) kept at electric potentials $V_{\rm tg}$, $V_{\rm bg}$ relative to TTG. **b**, Device A. **c**, Device B1. **d**, Device B2. **e**, Device C. **f**, Device D. **g**, Device E. **h**, Device F. R_{xx} and R_{yx} contacts used in this study are indicated by magenta dots for all devices. All scale bars are 3 μm.

Device	Approximate θ_{23}/θ_{12}	$\nu_{\rm m}$ of correlated states	Corresponding figure
Device A	2	$-1, -2, -3$	Fig. **2a**
Device B1	-2	8/3	Fig. **3a**
Device B2	-2	$-2, 1, 2, 3$	Extended Data Fig. **6b**
Device C	-3	$-2, 1, 2, 3$	Fig. **3b**
Device D	3	$-2, 1, 2, 3$	Extended Data Figs. **5a,b**
Device E	> 5	$-2, 1, 2, 3$	Extended Data Fig. **2a**
Device F	< -5	$-3, -2, 2, 3$	Extended Data Fig. **2b**

Extended Data Table 1. Summary of the correlated states observed at $B = 0$.

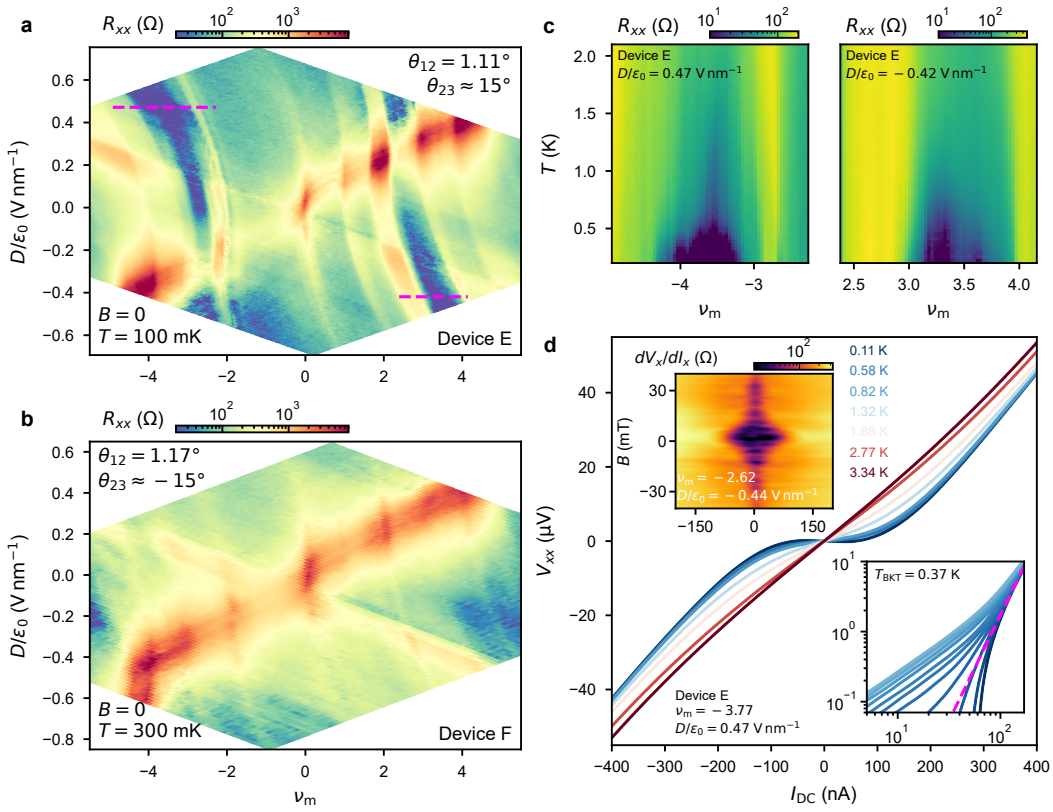

Extended Data Fig. 2. Correlated states and superconductivity in TTG with one graphene layer electronically decoupled. a, R_{xx} versus ν_m and D measured at $B = 0$ and $T = 300$ mK for Device E with $\theta_{12} = 1.11°, \theta_{23} \approx 15°$ (three layers of graphene helically twisted), showing resistance peaks at charge neutrality ($\nu_m = 0$), at the full filling of the first moiré bands ($\nu_m = \pm 4$), and at correlated states ($\nu_m = -2, 1, 2, 3$). The blue regions signal superconductivity. **b**, Same as **a**, measured at $T = 300$ mK for Device F with $\theta_{12} = 1.17°, \theta_{23} \approx -15°$ (three layers of graphene alternating twisted), showing correlated states with peaked R_{xx} at $\nu_m = \pm 2$. The lack of signatures for superconductivity is possibly due to the higher T or sample not having the optimal twist angle. **c**, R_{xx} versus ν_m and T measured for Device E along the magenta lines marked in **a**, demonstrating superconducting transitions on both electron- and hole-doped sides. Data is taken at $D/\epsilon_0 = 0.47$ V nm^{-1} (left) and -0.42 V nm^{-1} (right). **d**, V_{xx} versus I_{DC} curves at various T, measured in Device E. Data is taken at $\nu_m = -3.77$, $D/\epsilon_0 = 0.47$ V nm^{-1}. Bottom-right insets plot the same data in the log-log scale, sampled at finer temperature increments, where $T_{BKT} = 0.37$ K can be extracted. Top-left insets show differential resistance dV_x/dI_x versus I_{DC} and small perpendicular magnetic field B, demonstrating Josephson interference patterns, which are evidence for robust superconductivity.

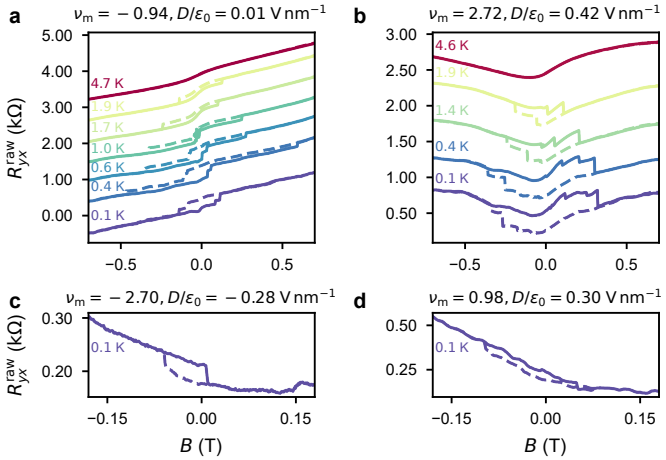

Extended Data Fig. 3. Field sweep measurements raw data. a-d, same as Figs. **2d-g**, only showing raw data R_{yx}, without antisymmetrization in magnetic field.

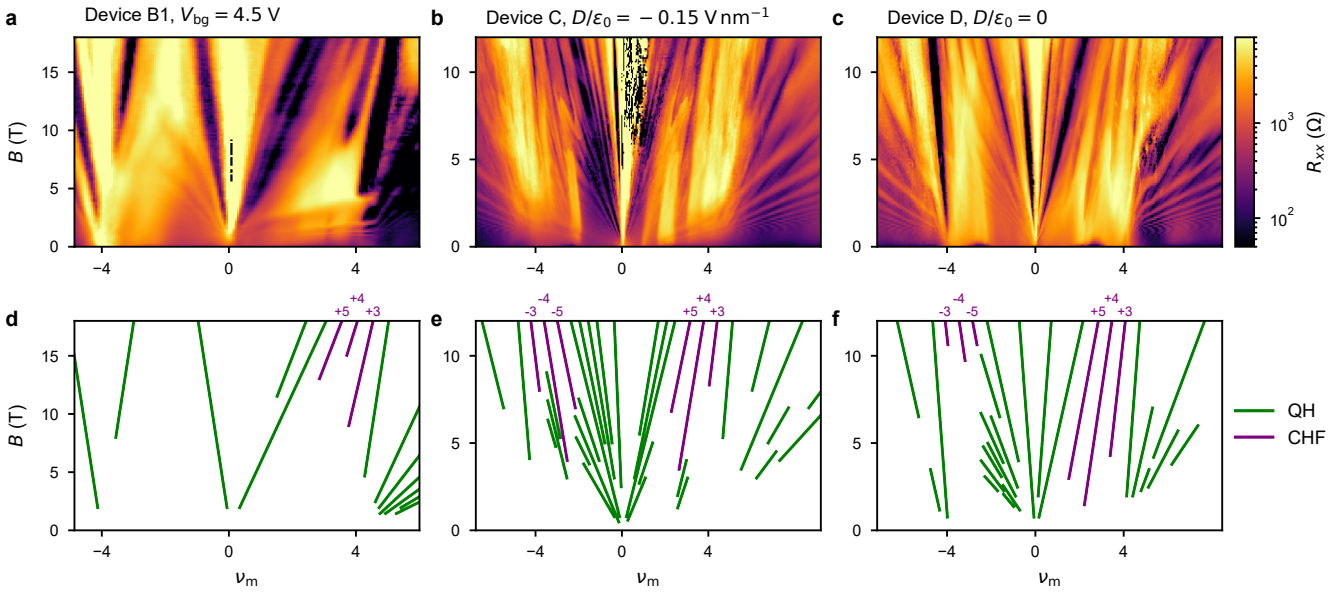

Extended Data Fig. 4. Landau fan diagram of quasicrystalline TTG. a-c, R_{xx} versus ν_m and B measured in quasicrystalline TTG devices shown in Fig. **3**, while keeping $V_{bg} = 4.5\,V$, $D/\epsilon_0 = -0.15\,V\,nm^{-1}$, and $D/\epsilon_0 = 0$, respectively. All data is taken in dilution refrigerators with mixing chamber temperature lower than 30 mK. **d-f**, Labels of main features in Landau fan diagrams shown in **a-c**, which are categorized into quantum hall states (QH) and correlated Hofstadter ferromagnetic states (CHF).

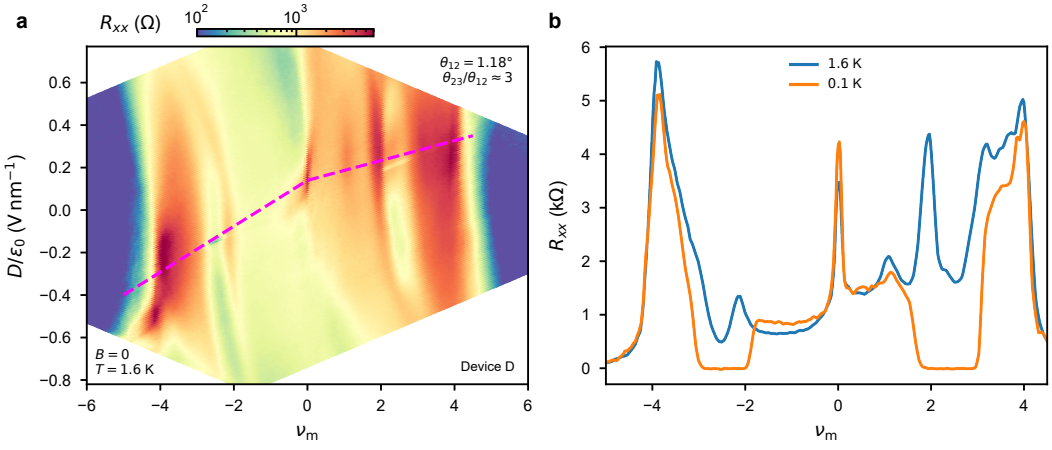

Extended Data Fig. 5. Correlated states in quasicrystalline TTG with $\theta_{23}/\theta_{12} \approx 3$. a, R_{xx} versus ν_m and D measured for Device D at $B = 0$ and $T = 1.6\,K$. Spin/valley degeneracy breaking states driven by electronic correlations manifest as R_{xx} peaks at $\nu_m = -2, 1, 2$ and 3. **b**, Line cuts of R_{xx} along the magenta line shown in **a**, plotted versus ν_m. Blue and orange curves are taken at $T = 1.6\,K$ and $T = 0.1\,K$, respectively. At lower temperature, most correlated states evolve into superconductivity.

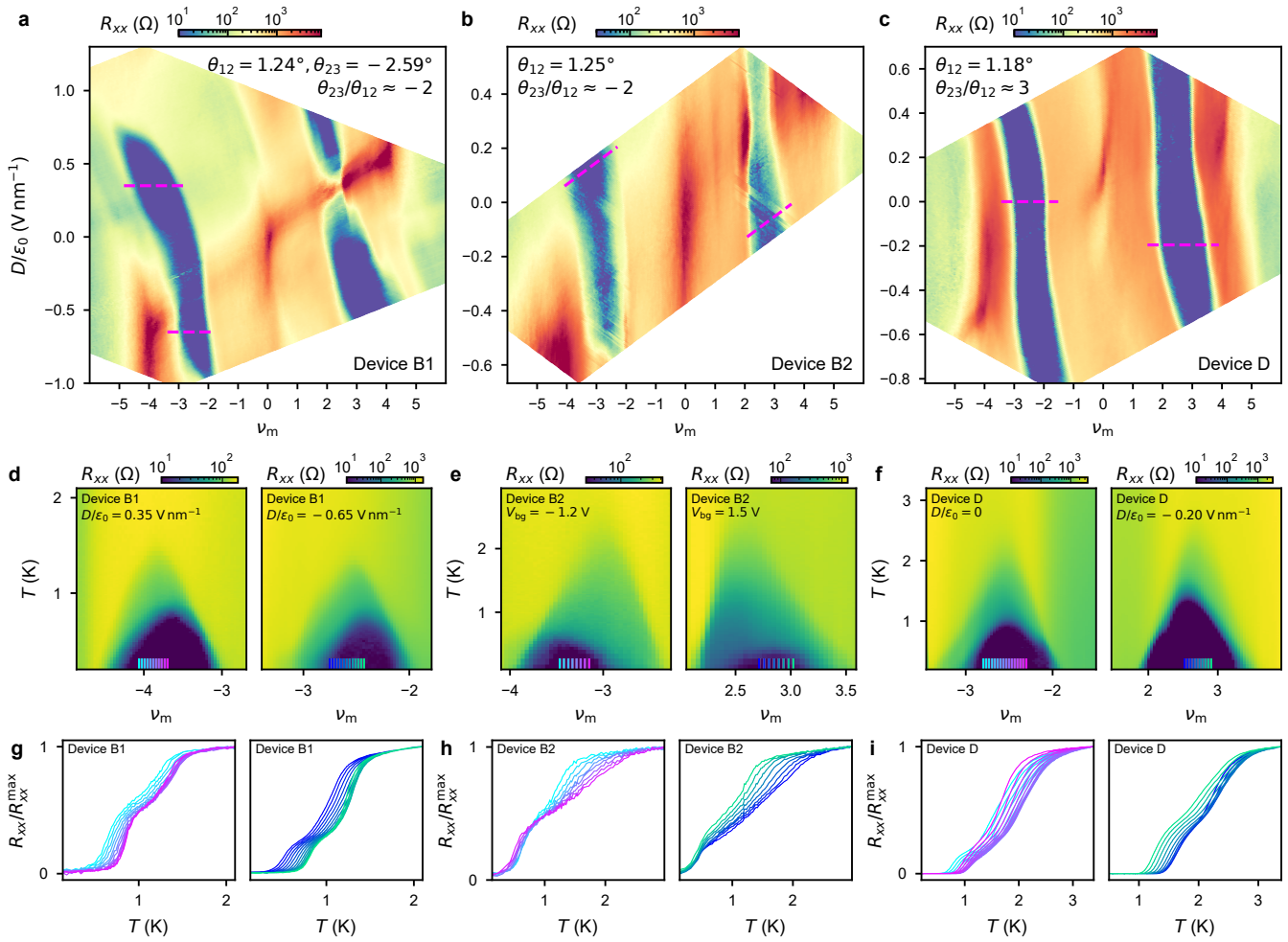

Extended Data Fig. 6. Ubiquitous two-dome structure of superconductivity in TTG devices with $\theta_{23}/\theta_{12} \approx -2$ and 3. a-c, R_{xx} versus ν_m and D measured at $B = 0$ and $T \approx 100$ mK for Device B1 (**a**), Device B2 (**b**), and Device D (**c**). Data in **a,c** is reproduced from Figs. **3a,c**. **d-f**, R_{xx} versus ν_m and T measured for Device B1, Device B2, and Device D along the magenta lines marked in **a-c**. All exhibit two-dome structures of the superconducting transition. **g-i**, R_{xx} versus T curves measured for Device B1 (**g**), Device B2 (**h**), and Device D (**i**), all illustrating two-step behaviour for the superconducting transition. The colours of the curves match the colours of the ticks at the bottom of **d-f**, indicating the ν_m and D where the data is taken.

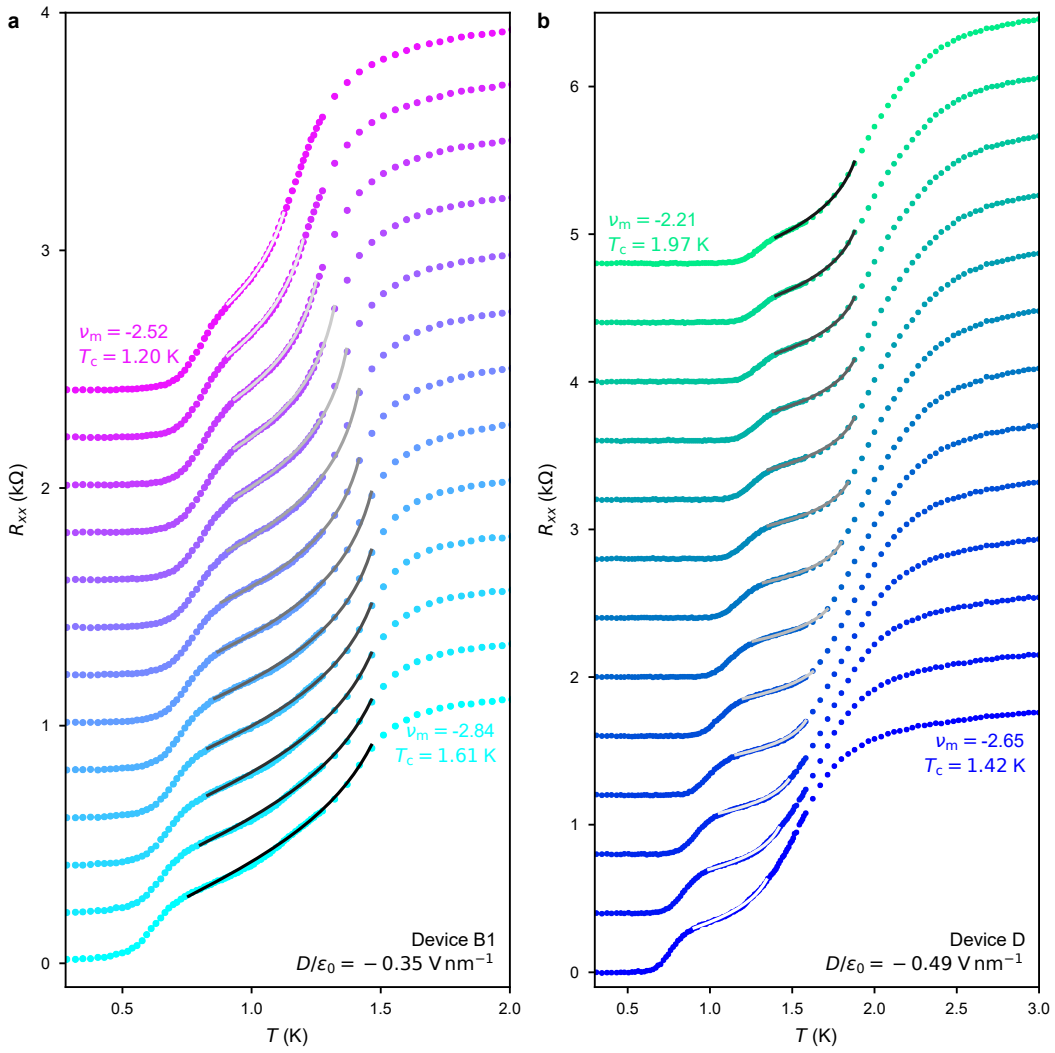

Extended Data Fig. 7. Superconducting proximity model fitting of $R_{xx}(T)$ traces between two transitions. **a**, $R_{xx}(T)$ traces reproduced from Fig. **4a**. Data taken at different ν_m is shifted by 0.2 kΩ. **b**, $R_{xx}(T)$ traces reproduced from Fig. **4b**. Data taken at different ν_m is shifted by 0.4 kΩ. Solid curves show the fitting results from the superconducting proximity model. The T_c values obtained from the fits are indicated for the first and last curves.

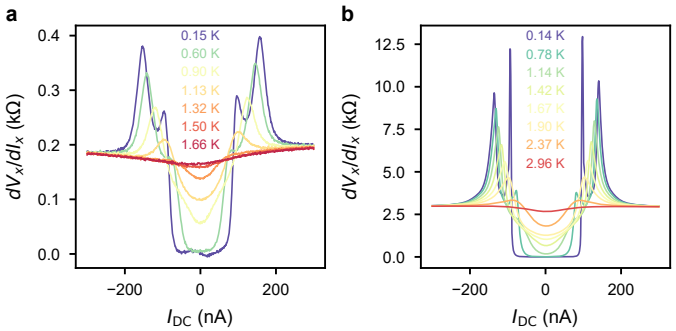

Extended Data Fig. 8. Temperature dependent differential resistance across superconducting transitions. **a,b**, dV_x/dI_x versus I_{DC} measured at different T. Data is reproduced from Figs. **4a,b**.

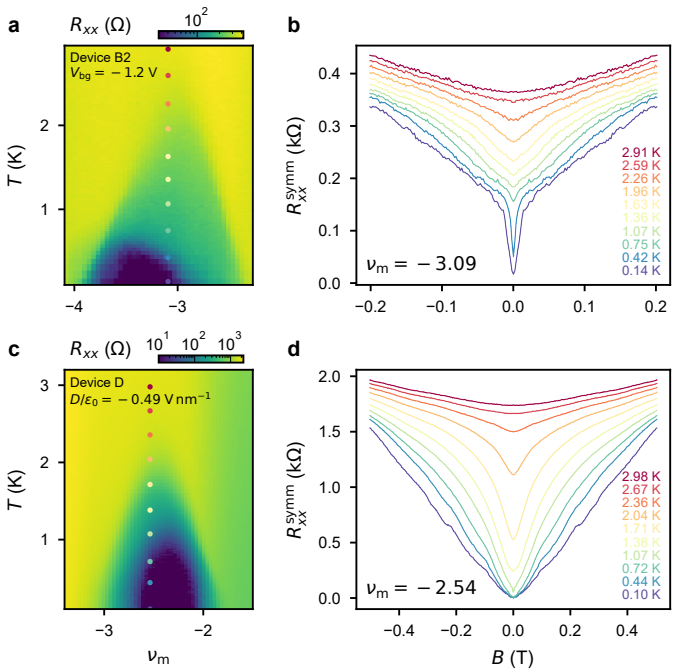

Extended Data Fig. 9. Temperature dependent magnetoresistance across superconducting transitions. a,c, R_{xx} versus ν_m and T measured for Device B2 at $V_{bg} = -1.2$ V (**a**) and Device D at $D/\epsilon_0 = -0.49$ V nm^{-1} (**c**). Measurements under the same conditions are also presented in Extended Data Fig. **6e** left and Fig. **3f** left, respectively. **c** and Fig. **3f** left are not identical, because they were taken in different measurement sessions and Device D changed slightly during the thermal cycle. However, key properties of the sample, including correlated states and robust superconductivity with the two-step transition behaviour, still remain. **b,d**, Magnetoresistance measured at different T. The measurement conditions for each curves shown in **b** (**d**) are indicated by dots with the same colour code in **a** (**c**). Between the two transitions, both samples demonstrate a linear magnetoresistance at small B, consistent with the behaviour of Josephson junction arrays with free-moving vortices. Here, to remove the contribution from R_{yx} mixing, we plot symmetrized magnetoresistance R_{xx}^{symm}, which is calculated from the the measured R_{xx} using the relation $R_{xx}^{\mathrm{symm}}(B) = (R_{xx}(B) + R_{xx}(-B))/2$.

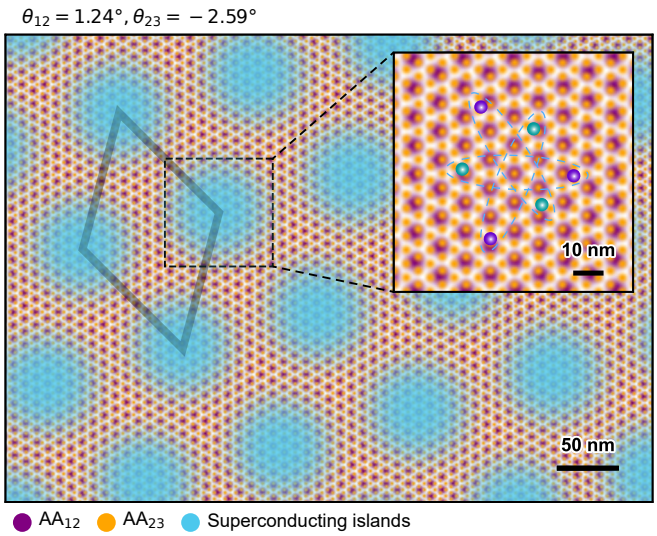

Extended Data Fig. 10. Schematic of supermoiré-modulated superconductivity in quasicrystalline TTG. Moiré AA sites and supermoiré unit cell are labelled as in Fig. **1b**. We use the twist angle values experimentally extracted for Device B1. Due to the supermoiré-modulated local electronic structure, certain regions in the supermoiré unit cell—such as $\mathbf{d} = \mathbf{0}$ shown here—can host superconductivity without global phase coherence between the two superconducting transitions. Inset shows zoomed-in illustration of the superconducting region, which is larger than or comparable to the size of Cooper pairs, given by the experimentally extracted Ginzburg–Landau coherence length.

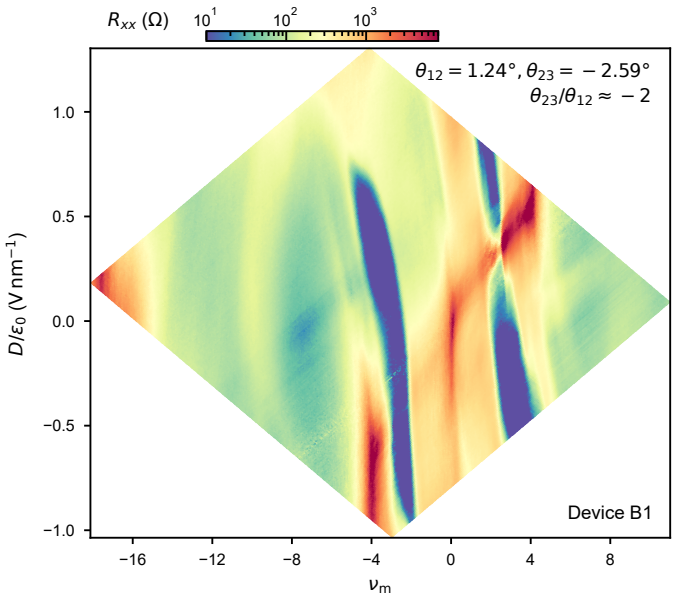

Extended Data Fig. 11. R_{xx} **versus** ν_m **and** D **measured for Device B1 with extended gate ranges.** Same measurement is presented in Fig. **3a**. From the R_{xx} peak at $\nu_m = -17.5$, we extract $|\theta_{23}| = 2.59°$.

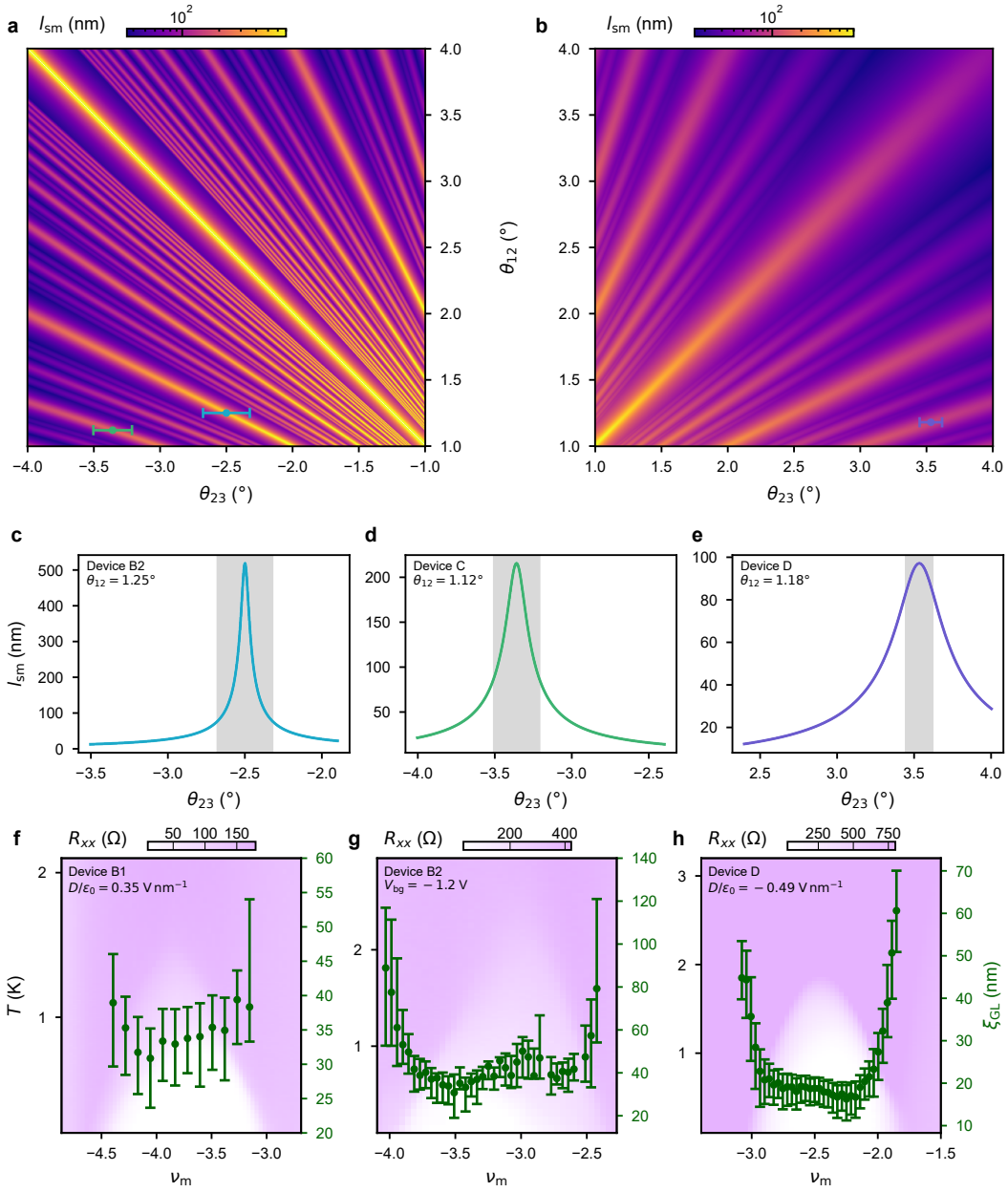

Extended Data Fig. 12. Comparison between supermoiré wavelength and Ginzburg-Landau coherence length. **a,b**, Calculated supermoiré wavelength as a function of θ_{12} and θ_{23} for alternating-twisted TTG (**a**) and helically-twisted TTG (**b**). See Methods F for calculation details. **c-e**, l_{sm} calculated using Eq. 2 as a function of θ_{23} for Device B2 (**c**), Device C (**d**), and Device D (**e**). Here, we use the experimental values of θ_{12} and targeted (p, q) in Eq. 2. Grey-shaded regions show the θ_{23} ranges for each device, which are estimated from the absence of R_{xx} peaks corresponding to the supermoiré density (see Methods C for details). These devices are marked in **a,b** using the same colour code, where the error bars are the estimated θ_{23} range. **f-h**, Extracted Ginzburg-Landau coherence length ξ_{GL} versus ν_m for Device B1 (**f**), Device B2 (**g**), and Device D (**h**). Colour maps show R_{xx} versus ν_m and T, reproduced from Extended Data Fig. **6d** left (**f**), Extended Data Fig. **6e** left (**g**), and Extended Data Fig. **9c** (**h**). See Methods G for details of ξ_{GL} extraction.